Univerzita Karlova v Praze
Matematicko-fyzikální fakulta

DIPLOMOVÁ PRÁCE

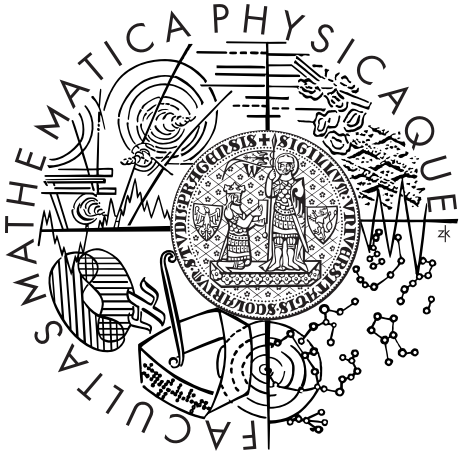

Bc. Attila Bartha

Studium magnetismu vrstevnatých tetragonálních sloučenin na bázi vzácných zemin a uranu

Katedra fyziky kondenzovaných látek

Vedoucí diplomové práce: RNDr. Marie Kratochvílová

Studijní program: Fyzika (N1701)

Studijní obor: FKSM (1701T041)

Praha 2015

Charles University in Prague
Faculty of Mathematics and Physics

MASTER THESIS

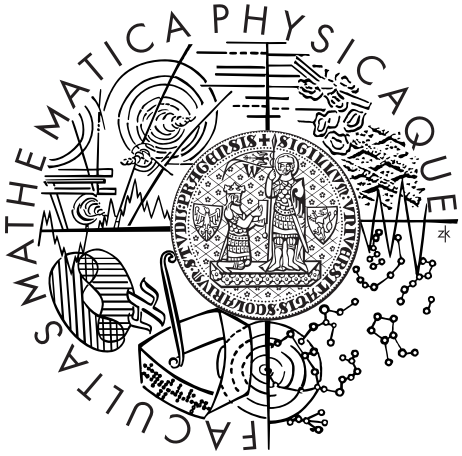

Bc. Attila Bartha

Magnetic study of layered tetragonal compounds based on rare earths and uranium

Department of Condensed Matter Physics

Supervisor of the master thesis:	RNDr. Marie Kratochvílová
Study program:	Fyzika (N1701)
Specialization:	FKSM (1701T041)

Prague 2015

First of all, I would like to express my honest gratitude to my supervisor RNDr. Marie Kratochvílová for her time, support and helpful guidance she devoted to me during my work. Further, I would like to thank doc. RNDr. Martin Diviš, Csc. for the theoretical calculations on both rare earth and actinide compounds studied within the scope of this work. Then I would like to thank Mgr. Petr Čermák, Ph.D., who helped to realize the neutron diffraction measurements and the subsequent data evaluation. Special thanks also belongs to prof. RNDr. Vladimír Sechovský, DrSc. and Dr. rer. nat Jeroen Custers for their valueable advices and suggestions. I would also like to thank RNDr. Michal Vališka, RNDr. Jaroslav Valenta and Ing. Barbora Vondráčková for their help provided during measurements of thermal expansion, electrical resistivity under hydrostatic pressure and sample preparation, respectively.

Last but not least, I would like to thank my family and friends who gave their unconditional support for the successful completion of my thesis.

I declare that I carried out this master thesis independently, and only with the cited sources, literature and other professional sources.

I understand that my work relates to the rights and obligations under the Act No. 121/2000 Coll., the Copyright Act, as amended, in particular the fact that the Charles University in Prague has the right to conclude a license agreement on the use of this work as a school work pursuant to Section 60 paragraph 1 of the Copyright Act.

In ..... date ..... signature of the author

Název práce: Studium magnetismu vrstevnatých tetragonálních sloučenin na bázi vzácných zemin a uranu

Autor: Bc. Attila Bartha

Katedra: Katedra fyziky kondenzovaných látek

Vedoucí diplomové práce: RNDr. Marie Kratochvílová

Abstrakt: Zabývali jsme se studiem vlivu vrstevnaté krystalové struktury na magnetizmus $5f$ elektronů v tetragonálních uranových sloučeninách $U_n T In_{3n+2}$. Monokrystaly sloučenin U_2RhIn_8, $URhIn_5$ a UIn_3 byly připraveny pomocí růstu z indiového roztoku. Nová fáze U_2RhIn_8 krystalizuje ve struktuře typu Ho_2CoGa_8 s mřížovými parametry $a = 4.6056(6)$ Å a $c = 11.9911(15)$ Å. Vlastnosti U_2RhIn_8 jsou blízké příbuzným materiálům $URhIn_5$ a UIn_3, jak ukázala měření magnetizace, měrného tepla a elektrického odporu. Výjimkou je pouze výrazná magnetokrystalová anizotropie ternárních sloučenin vůči kubické fázi UIn_3. U_2RhIn_8 se uspořádává antiferomagneticky pod teplotou $T_N = 117$ K s mírně zvýšeným Sommerfeldovým koeficientem $\gamma = 47$ mJ·mol^{-1}·K^{-2}. Teplota přechodu roste s rostoucím poměrem mřížových parametrů c/a, vykazuje tedy opačné chování oproti příbuzným cérovým materiálům $Ce_n T In_{3n+2}$. Vliv magnetické pole na teplotu uspořádání je v případě obou ternárních sloučenin zanedbatelný až do 9 T. Naopak působením hydrostatického tlaku hodnota T_N roste až do maximálního dosaženého tlaku 3.2 GPa a koeficient růstu $\partial T_N/\partial p$ odpovídá chování příbuzných systémů $URhIn_5$ a UIn_3. Teplotní roztažnost krystalu U_2RhIn_8 vykazuje hysterezní chování antiferomagnetického přechodu, což odpovídá přechodu prvního druhu. Neutronová difrakce odhalila, že magnetická struktura sloučeniny $URhIn_5$ se propaguje s vektorem $\boldsymbol{k} = (^1/_2, ^1/_2, ^1/_2)$ a zjištěný magnetický moment dosahuje hodnoty $\mu = 1.65\ \mu_B$/U.

Klíčová slova: růst z roztoku, $5f$ magnetizmus, vrstevnatá tetragonální struktura, U_2RhIn_8, magnetická struktura

Title: Magnetic study of layered tetragonal compounds based on rare earths and uranium

Author: Bc. Attila Bartha

Department: Department of Condensed Matter Physics

Supervisor: RNDr. Marie Kratochvílová

Abstract: We have studied the interplay between the layered crystal structure and the $5f$ magnetism in uranium-based tetragonal compounds $U_n T In_{3n+2}$. Single crystals of U_2RhIn_8, $URhIn_5$ and UIn_3 were prepared by In self-flux method. The novel U_2RhIn_8 compound adopts the Ho_2CoGa_8-type structure with lattice parameters $a = 4.6056(6)$ Å and $c = 11.9911(15)$ Å. The behavior of U_2RhIn_8 strongly resembles that of related $URhIn_5$ and UIn_3 with respect to magnetization, specific heat and electrical resistivity except for magnetocrystalline anisotropy developing on stacking composition in the series UIn_3 vs. U_2RhIn_8 and $URhIn_5$. U_2RhIn_8 orders antiferromagnetically below $T_N = 117$ K and exhibits slightly enhanced Sommerfeld coefficient $\gamma = 47$ mJ·mol^{-1}·K^{-2}. T_N increases with increasing c/a ratio in contrast to the behavior of their $Ce_n T In_{3n+2}$ counterparts. Magnetic field leaves the value of the Néel temperature of $URhIn_5$ and U_2RhIn_8 unaffected up to 9 T. On the other hand, T_N increases with applied hydrostatic pressure up to 3.2 GPa with the $\partial T_N/\partial p$ coefficient resembling $URhIn_5$ and UIn_3. Thermal expansion of U_2RhIn_8 reveals a hysteretic behavior of the antiferromagnetic transition pointing to its 1st-order character. The magnetic structure of $URhIn_5$ obtained from neutron diffraction propagates with $\boldsymbol{k} = (^1/_2, ^1/_2, ^1/_2)$ and the magnetic moment $\mu = 1.65\ \mu_B$/U.

Keywords: growth from solution, $5f$ magnetism, tetragonal layered structure, U_2RhIn_8, magnetic structure

Contents

1. Introduction

1.1 Motivation and Aim

In this thesis we studied the synthesis and physical properties of uranium-based layered tetragonal compounds described by a general formula $U_n T_m X_{3n+2m}$ (T = transition metal; X = p-metal; n = 1, 2; m = 0, 1). These materials are isostructural with the thoroughly studied cerium-based compounds to which for example the well-known representant $CeRhIn_5$ [7] belongs. The compounds crystallize in the $Ho_nCo_mGa_{3n+2m}$ tetragonal structure with the space group P4/mmm (No. 123). The UX_3 compounds (n = 1, m = 0) crystallize in the cubic $AuCu_3$-type structure with space group $Pm\bar{3}m$ (group No. 221) with a purely three-dimensional arrangement of uranium atoms. The tetragonal crystal structure consists of m layers of TIn_2 alternating with n layers of UIn_3 along the tetragonal c-axis. The successful preparation of $URhIn_5$ compound [1, 2] parallelly with a Japanese group [1] motivated us to prepare a broad range of compounds with different layer stacking, in order to investigate the effect of stacking composition on $5f$ magnetism and the anisotropic properties. The following section offers a concise overview of physical properties of previously studied cerium-based heavy fermion compounds as well as uranium compounds within the $U_n T X_{3n+2}$ family.

The Ce-based heavy fermion compounds, which are isostructural with the uranium compounds studied within this work, form an interesting group represented by a general formula $Ce_n T_m In_{3n+2m}$. The layered structure of these compounds allows the investigation of 'dimensionality' effect on physical properties. Adding a layer of TIn_2 moves the character from 3D to more 2D-like. In the case of $Ce_n T_m In_{3n+2m}$ the 'dimensionality' proved itself to be a powerful tuning parameter; the superconducting transition temperature gradually increases while moving from 3D to more 2D-like structure. The physical properties of selected compounds are discussed in detail further in the text.

The simplest case is $CeIn_3$, where the cerium atoms have a fully 3D arrangement (see Figure 1.1). This compound orders antiferromagnetically at T_N = 10 K with a propagation vector $\boldsymbol{k} = (^1/_2, ^1/_2, ^1/_2)$ [3]. With applied pressure of 2.8 GPa it undergoes a superconducting transition at T_{SC} = 0.18 K [4].

$CeCoIn_5$ and $CeIrIn_5$ are well-known heavy fermion superconductors with transition temperatures T_{SC} = 2.3 K and 0.4 K, respectively [5]. $CeRhIn_5$ orders antiferromagnetically below the Néel temperature T_N = 3.8 K and becomes superconducting at T_{SC} = 2.2 K under applied pressure p = 1.63 GPa [6]. The magnetic structure of $CeRhIn_5$ (without external magnetic field) is incommensurate with a propagation vector $\boldsymbol{k} = (^1/_2, ^1/_2, 0.297)$ [7].

All the $CeTIn_5$ compounds have Ce_2TIn_8 relatives (see Figure 1.1), which reflect somewhat their ground state properties according to the corresponding transition metal. However, due to reduced dimensionality effect in the $CeTIn_5$ compounds, the phase transition temperatures in Ce_2TIn_8 are generally lower. Ce_2CoIn_8 shows a superconducting transition at T_{SC} = 0.4 K [8]. Ce_2IrIn_8 is a heavy fermion paramagnet, as it does not show any superconducting transition down to 50 mK [9]. Ce_2RhIn_8 orders antiferromagnetically at T_N = 2.8 K. This

compound becomes superconducting at $T_{SC} \simeq 400$ mK under applied pressure of 1.1 GPa [10]. The magnetic structure of Ce_2RhIn_8 is commensurate with a propagation vector $\boldsymbol{k} = (^1/_2, ^1/_2, 0)$ [11].

UX_3 compounds

The crystal structure of UX_3 (X = Al, Si, Ge, Ga, In, Sn, Tl, Pb) compounds is shown in Figure 1.1.

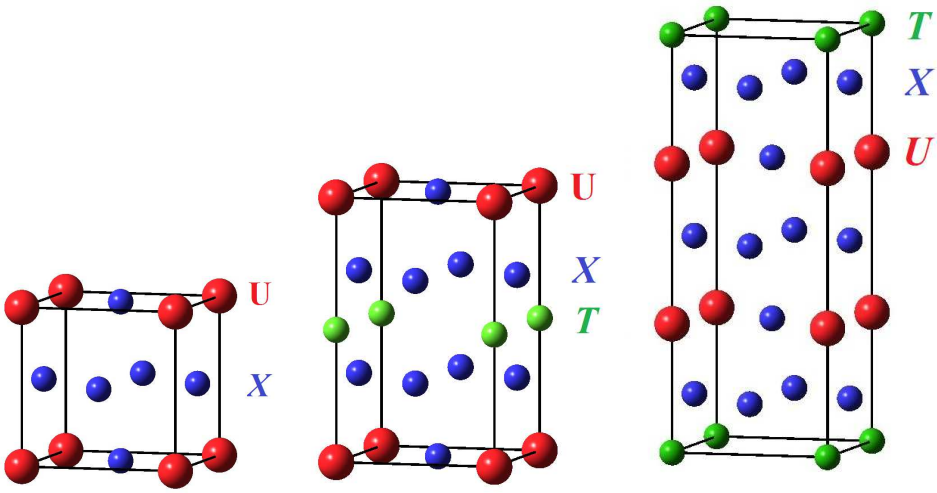

Figure 1.1: Crystal structure of $U_n T X_{3n+2}$ compounds.

Considering UX_3 (X = p-metal) compounds, the size of the p-atom is a crucial parameter. In case of smaller X-ions (Si, Ge) lack of magnetic ordering (USi_3, UGe_3 [12, 13]) is observed due to strong $5f$-p hybridization (for details see Section 2.6). On the other hand, larger X-ions cause the hybridization to be weaker, resulting in a magnetic ground state (UIn_3, UPb_3 [14, 15]). Figure 1.2 shows lattice parameters and ordering temperatures for UX_3 compounds as a function of atomic number. The physical properties of selected materials are discussed below in detail.

- The compounds UAl_3, USi_3 and UGe_3 show enhanced Pauli-like paramagnetism down to the lowest temperature accessible by experimental technique [12, 13, 16].

- USn_3 is on the verge of magnetic instability but does not order magnetically. It shows a temperature independent magnetic susceptibility at low temperatures and a rather high Sommerfeld coefficient $\gamma = 169$ mJ·mol^{-1}·K^{-2} [17].

- UGa_3 is an itinerant spin-density-wave-type antiferromagnet with ordering temperature $T_N = 67$ K [16]. Increasing hydrostatic pressure causes a monotonous decrease of Néel temperature with a rate of -1.4 K·GPa^{-1}.

- UIn_3 orders antiferromagnetically with a rather high ordering temperature $T_N = 88$ K. Application of hydrostatic pressure increases the value of T_N to 127 K at 9 GPa [18]. Neutron experiments revealed the propagation vector $\boldsymbol{k} = (^1/_2, ^1/_2, ^1/_2)$ [14] similarly to $CeIn_3$ [3].

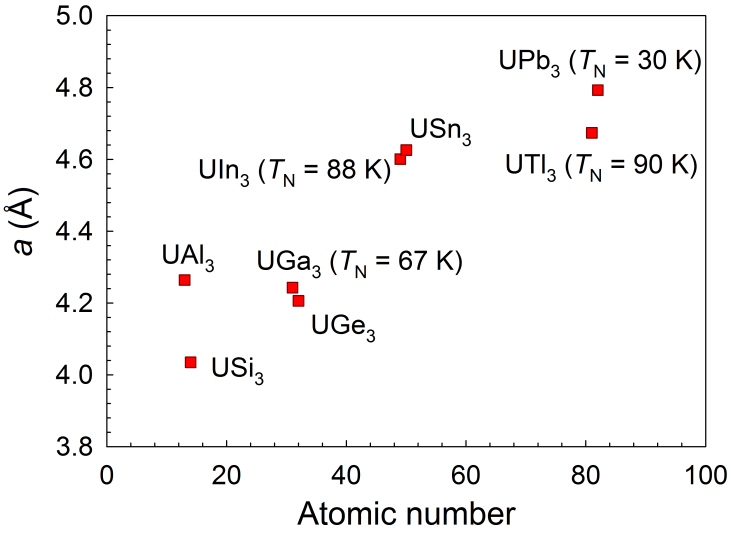

Figure 1.2: Lattice parameters and ordering temperatures for UX_3 compounds as a function of atomic number [14].

- UTl_3 orders antiferromagnetically with $T_N = 90$ K and shows a local moment behavior [13].
- UPb_3 also shows antiferromagnetic ordering ($T_N = 30$ K). The magnetic structure of UPb_3 is described with a propagation vector $\boldsymbol{k} = (0, 0, {}^1/_2)$ [15].

UTX_5 compounds

Adding a layer of $T\mathrm{In}_2$ between the UIn_3 'blocks' creates the UTX_5 (according to their stoichiometry simply called '115') compounds. The crystal structure is shown in Figure 1.1. Table 1.1 shows the lattice parameters of UTX_5 compounds. The physical properties are discussed below.

	Ni	Pd	Pt	Fe	Co	Ir	Rh	Rh*
a (Å)	4.238	4.322	4.339	4.261	4.233	4.317	4.299	4.621
c (Å)	6.786	6.864	6.805	6.734	6.723	6.745	6.800	7.417

Table 1.1: Lattice parameters of UTX_5 compounds [1, 19, 20]. Rh* marks the lattice parameters of $URhIn_5$ compound measured by Matsumoto *et al.* [1].

- $UNiGa_5$, $UPdGa_5$ and $UPtGa_5$ are itinerant antiferromagnets with ordering temperatures $T_N = 86$ K, 30 K and 26 K, respectively [21]. The propagation vector $\boldsymbol{k} = ({}^1/_2, {}^1/_2, {}^1/_2)$ for $UNiGa_5$ and $\boldsymbol{k} = (0, 0, {}^1/_2)$ in the case of $UPdGa_5$ and $UPtGa_5$ was found by neutron diffraction measurements [20]. The ordered moment changes from 0.9 μ_B in $UNiGa_5$ to 0.24 μ_B in $UPtGa_5$.
- $UFeGa_5$, $UCoGa_5$, $URhGa_5$ and $UIrGa_5$ compounds do not show any magnetic ordering throughout the whole temperature range [20].

UTIn$_5$ has only one representative compound, URhIn$_5$. In contrast to its non-magnetic counterpart ThRhIn$_5$, URhIn$_5$ is an antiferromagnet with $T_{\mathrm{N}} = 98$ K. Magnetization measurements revealed huge magnetocrystalline anisotropy and an extremely large paramagnetic Curie temperature θ_{p} = -400 K with effective magnetic moment corresponding to a localized uranium ion. From the heat capacity measurements a moderately large Sommerfeld coefficient $\gamma = 50$ mJ·mol^{-1}·K^{-2} was obtained demonstrating the contribution of $5f$ electrons to the conduction band. A crossover from the high-temperature localized to a low-temperature itinerant character occurs around $T \sim 150$ K where the magnetic susceptibility and electrical resistivity show a marked anomaly. Increasing hydrostatic pressure supports the robustness of the antiferromagnetic phase [1].

U$_2$$\boldsymbol{T}$$\boldsymbol{X}$$_8$ compounds

By adding a 'block' of UIn$_3$ to the '115' compounds we create the U$_2$$TX_8$ (according to their stoichiometry '218') compounds. The crystal structure is shown in Figure 1.1.

Only two compounds with the '218' stoichiometry have been reported so far: U$_2$FeGa$_8$ and U$_2$RhGa$_8$. Both compounds are Pauli paramagnets and possess a relatively large Sommerfeld coefficient $\gamma = 52$ mJ·mol^{-1}·K^{-2} for U$_2$FeGa$_8$ and $\gamma = 43$ mJ·mol^{-1}·K^{-2} for U$_2$RhGa$_8$, respectively [22].

2. Magnetism of f-electron systems

2.1 Basic concepts

The magnetic properties of the materials stem almost solely from the motion of electrons. This motion which is the sum of electron spin and orbital motion, generates a magnetic moment connected with the electron. Classical electrodynamics equates the orbital motion of electrons with electrical current I flowing in infinitesimally small oriented loop enclosing the area $|\mathbf{dS}|$ (see Figure 2.1). The magnetic moment $\mathbf{d}\mu$ is given by

$$\mathbf{d}\mu = I\mathbf{dS}. \tag{2.1}$$

The units of $\mathbf{d}\mu$ are A.m^2. The vector of the magnetic moment $\mathbf{d}\mu$ is always perpendicular to the loop. The angular momentum of the electron orbiting the loops is known as orbital angular momentum. To be able to describe magnetic

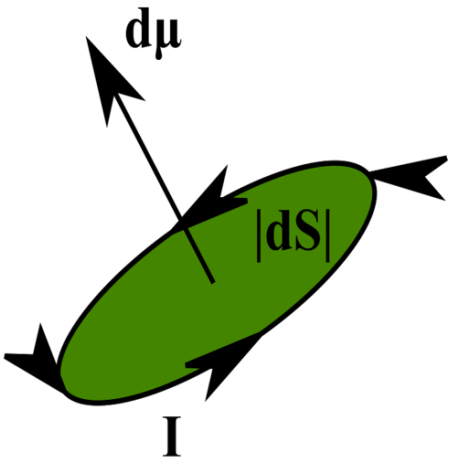

Figure 2.1: Infinitesimally small magnetic moment $\mathbf{d}\mu$ generated by electrical current I around oriented loop $\mathbf{dS}$.

properties of solid state systems, one has to leave the mechanical approach and move to the quantum one. Within this approach electron possesses another angular momentum called spin. The spin is an intrinsic degree of freedom, described by spin quantum number $s = \pm\frac{1}{2}$. In the language of quantum mechanics, one can define the operator of total orbital angular momentum $\mathbf{L}$ as follows

$$\hbar\mathbf{L} = \sum_i \mathbf{r}_i \times \mathbf{p}_i, \tag{2.2}$$

where the sum is over all the electrons in the atom, $\hbar$ is the Planck's constant and $\mathbf{r}_i$ points to a location of the i^{th} electron with the momentum of $\mathbf{p}_i$. We consider now an unperturbed Hamiltonian [23] $\hat{\mathcal{H}}_0$ as

$$\hat{\mathcal{H}}_0 = \sum_{i=1}^{Z}\left(\frac{\mathbf{p}_i^2}{2m_e} + V_i\right), \tag{2.3}$$

where Z is the number of electrons in the atom and m_e ($= 9.109382{\cdot}10^{-31}$ kg) is the electron mass. The first term in 2.3 represents the kinetic energy and V_i is the potential energy of the i^{th} electron [23]. After the application of external magnetic field $\mathbf{B}$, the unperturbed Hamiltonian $\hat{\mathcal{H}}_0$ is modified as

$$\begin{aligned}\hat{\mathcal{H}} &= \sum_{i=1}^{Z}(\frac{\mathbf{p}_i^2}{2m_e} + V_i) + \mu_{\text{B}}(\mathbf{L} + g\mathbf{S})\cdot\mathbf{B} + \frac{e^2}{8m_e}\sum_{i=1}^{Z}(\mathbf{B}\times\mathbf{r}_i)^2 \\ &= \hat{\mathcal{H}}_0 + \mu_{\text{B}}(\mathbf{L} + g\mathbf{S})\cdot\mathbf{B} + \frac{e^2}{8m_e}\sum_{i=1}^{Z}(\mathbf{B}\times\mathbf{r}_i)^2\end{aligned} \tag{2.4}$$

where e is the elementary charge of the electron, g is the so-called g-factor which takes a value of ~ 2 and $\mathbf{S}$ is the total spin angular momentum defined using the Pauli spin matrices [23] σ as $\mathbf{S} = \frac{1}{2}\,\sigma$. Equation 2.4 describes the origin of the free magnetic moment in applied magnetic field as a sum of three contributions: unperturbed Hamiltonian $\hat{\mathcal{H}}_0$ followed by the paramagnetic and diamagnetic contributions.

In equation 2.4 a new, convenient physical unit was introduced for measuring atomic magnetic moments: the Bohr magneton μ_{B}. It is defined as $\mu_{\text{B}} = \frac{e\hbar}{2m_e}$ ($= 9.27{\cdot}10^{-24}$ A.m^2).

In order to further discuss the role of paramagnetic and diamagnetic contributions to the total magnetic moment, one needs to define physical quantities – magnetization $\mathbf{M}$ and magnetic susceptibility χ. Magnetization $\mathbf{M}$ is defined as magnetic moment per unit volume and in the SI system has a unit of A$\cdot$m^{-1}. Considering a linear response to magnetic field, one can introduce a dimensionless quantity called magnetic susceptibility χ as $\mathbf{M} = \chi\mathbf{H}$, where $\mathbf{H} = \mu_0\mathbf{B}$ and μ_0 $= 4\pi\cdot 10^{-7}$ H$\cdot$m^{-1} is the permeability of vacuum. Magnetic susceptility χ gives information about the degree of magnetization in the material in the presence of applied magnetic field.

Diamagnetism

Diamagnetism refers to substances with negative magnetic susceptibility χ. From a classical point of view it can be interpreted using Lenz's law which states that the applied magnetic field induces magnetic moments which oppose the field that created them [24]. Diamagnetism is a purely quantum mechanical phenomenon and is represented as the last term in equation 2.4. Considering the case when $\mathbf{L} = \mathbf{S} = 0$, all the atomic shells are fully occupied and using 1$^{\text{st}}$-order perturbation theory, one can calculate the diamagnetic susceptibility χ_{dia} as

$$\chi_{\text{dia}} = \frac{M}{H} = -\frac{Ne^2\mu_0}{6Vm_e}\sum_{i=1}^{Z}\langle\mathbf{r}_i^2\rangle, \tag{2.5}$$

In equation 2.5, N is a number of ions with Z electrons occupying a volume V and $\langle\mathbf{r}_i^2\rangle$ is a root mean square ionic radius. Diamagnetic susceptibility gives a temperature independent negative contribution to the materials response in applied magnetic field which is present in all materials. Superconducting materials are often referred to as perfect diamagnets [25], due to Meissner-Ochsenfeld effect [26], with a diamagnetic susceptibility $\chi_{\text{dia}} = -1$. Typical examples of diamagnetic materials are inert gases, metals such as mercury (Hg), copper (Cu) and bismuth (Bi) or water (H_2O).

Paramagnetism

Paramagnetism emerges in ions with non-zero **L** or **S** (or both). Diamagnetic materials contain no unpaired electrons, thus the ions have no magnetic moment in the absence of applied magnetic field. Paramagnetic materials contain unpaired electrons which are the sources of magnetic moments irrespective to magnetic field. These magnetic moments point in random directions without applied magnetic field and yield positive magnetic susceptibility. Applied magnetic field **B** aligns these independent moments into the direction of the magnetic field. On the other hand, increased temperature T serves the opposite purpose, i.e. randomizes the direction of moments, therefore the paramagnetic response of a material is proportional to $\frac{B}{T}$ ratio.

Quantum mechanical treatment of paramagnetism (second term in equation 2.4) states that magnetization is linearly proportional to Brillouin function B_{J}

$$M = M_{\mathrm{s}} B_{\mathrm{J}}(y), \tag{2.6}$$

where M_{s} is saturation magnetization and $B_{\mathrm{J}}(y)$ is defined as

$$B_{\mathrm{J}}(y) = \frac{2J+1}{2J}\coth(\frac{2J+1}{2J}y) - \frac{1}{2J}\coth\frac{y}{2J}. \tag{2.7}$$

In the argument $y = \frac{g_{\mathrm{J}}\mu_{\mathrm{B}}JB}{k_{\mathrm{B}}T}$, g_{J} is the Landé g-factor, J is the total angular momentum quantum number and k_{B} is the Boltzmann constant. In the case of small magnetic fields, the paramagnetic susceptibility takes the value

$$\chi_{\mathrm{para}} = \frac{n\mu_0\mu_{\mathrm{eff}}^2}{3k_{\mathrm{B}}T} = \frac{C}{T}, \tag{2.8}$$

where n denotes the number of magnetic moments per unit volume and C is the Curie constant. Equation 2.8 is called the Curie law and allows the deduction of the value of effective magnetic moment μ_{eff}

$$\mu_{\mathrm{eff}} = g_{\mathrm{J}}\mu_{\mathrm{B}}\sqrt{J(J+1)} \tag{2.9}$$

from a measurement of the materials response in a small magnetic field. Measurements in high magnetic fields leads to saturation magnetization

$$M_{\mathrm{s}} = ng_{\mathrm{J}}\mu_{\mathrm{B}}J. \tag{2.10}$$

Hund's rules

Electrons in atoms are distributed within filled and unfilled atomic shells. The completely filled shells ($\mathbf{L} = \mathbf{S} = 0$) do not contribute to the total angular momentum **J**, whereas electrons in unfilled shells can give a non-zero contribution to the total angular momentum. Hund's rules is a set of empirical statements which finds the most favourable configuration that minimizes the total energy.

The first rule states the one should arrange the wave function in order to maximize the quantum number of the total spin angular momentum **S**. This is the consequence of the Pauli exclusion principle which prevents two electrons with parallel spins occupying the same place, thus minimizing the Coulomb repulsion.

The second rule maximizes L, the quantum number of the total orbital angular momentum **L**. This rule also reduces the Coulomb repulsion since electrons orbiting in the same direction can avoid each other more effectively.

The third rule defines the value of J, the quantum number of total angular momentum $\mathbf{J}$, as $J = |L - S|$ for atomic shells less than half-filled and $J = |L + S|$ for more than half-filled shells. This rule attempts to minimize the spin-orbit coupling. In rare earth ions the concept of Hund's rules works well due to the localized character of $4f$ wave functions. On the other hand, in transition metals, due to dominant crystal field interaction which quenches the orbital moments, Hund's rules are not applicable and different theory is used.

Hund's rules give information about ground state, but do not discuss the excited states. Ground state of an ion can be summarized by term symbols ${}^{2S+1}L_J$. They also allow us to estimate the value of effective magnetic moment μ_{eff} using equation 2.9.

2.2 Localized and itinerant electron magnetism

Magnetic properties of (inter)metallic compounds can be described within the framework of two basic approaches: the local moment and itinerant electron model. These models only mimic the reality and can be be used in limit cases. The following paragraphs will give a brief overview of the basics of these approaches [27, 28].

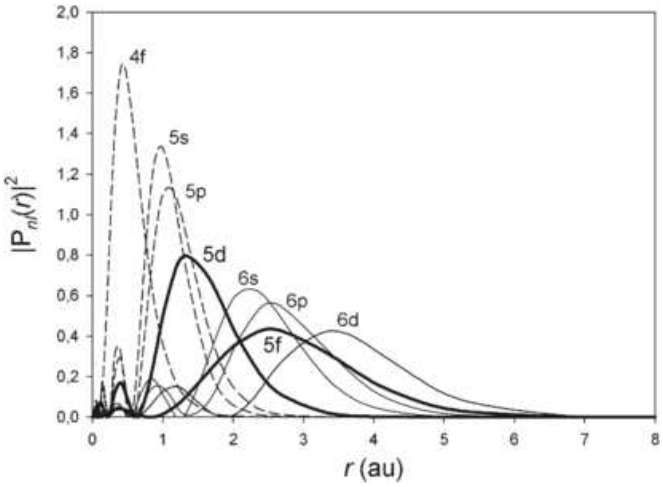

Figure 2.2: Schematic sketch of radial wave functions. Taken from [29].

Localized electron magnetism

This type of behavior is characteristic for magnetic moments of well localized electrons. The localization criterion is satisfied for $4f$ electrons (lanthanide series) where the $4f$ wave function lies deeply embedded in the core of the atom (see figure 2.2) and does not contribute to conduction or chemical bonding. The foundations of this model are based on the well localized $4f$ wave functions which allow a nearly free ion character due to negligible spatial overlap. As a result, the observed effective magnetic moments are close those expected from Hund's rules (equation 2.9). The behavior of a localized system can be described using a full free ion Hamiltonian

$$\hat{\mathcal{H}} = \hat{\mathcal{H}}_0 + \hat{\mathcal{H}}_{\text{res}} + \hat{\mathcal{H}}_{\text{SO}} + \hat{\mathcal{H}}_{\text{CF}}, \tag{2.11}$$

where

$$\hat{\mathcal{H}}_0 = \sum_{i=1}^{Z}(\frac{\mathbf{p}_i^2}{2m_e} - \frac{Ze^{,2}}{r_i} + V_{\mathrm{ef}}(\mathbf{r}_\mathrm{i})),\ \ e^{,2} = \frac{e^2}{4\pi\epsilon_0}, \tag{2.12}$$

with contributions of kinetic (first) term, the electrostatic potential of nuclei is represented by the second term and the effective potential $V_{\mathrm{ef}}(\mathbf{r}_\mathrm{i})$, Coulomb and exchange interaction from Hartree-Fock approximation, is given by the third term in equation 2.12. Residual interaction $\hat{\mathcal{H}}_{\mathrm{res}}$ is a perturbation which takes the form

$$\hat{\mathcal{H}}_{\mathrm{res}} = \sum_{i\neq j}\frac{e^{,2}}{\mid \mathbf{r}_\mathrm{i} - \mathbf{r}_\mathrm{j} \mid} - \sum_{i=1}^{Z} V_{\mathrm{ef}}(\mathbf{r}_\mathrm{i}), \tag{2.13}$$

that includes e-e interaction (first term) and the effective potential (second term). Besides electrostatic interactions the free ion Hamiltonian contains magnetic interactions such as spin-orbit interaction $\hat{\mathcal{H}}_{\mathrm{SO}}$. It is a relativistic effect, describing the coupling of spin and orbital angular momenta **S** and **L** and it is the predominant interaction described by Hamiltonian:

$$\hat{\mathcal{H}}_{\mathrm{SO}} = \sum_{i=1}^{N}\xi(r_i)(\mathbf{s}_i \cdot \mathbf{l}_i), \tag{2.14}$$

where the spin-orbit parameter $\xi(r)$ is given by [27]

$$\xi(r_i) = \frac{\hbar^2}{2m_e^2c^2}\frac{1}{r_i}\frac{\mathrm{d}U}{\mathrm{d}r_i}, \tag{2.15}$$

where c is the speed of light and U is a spherically symmetric effective potential.

Crystal electric field (CEF) is a consequence of charge distribution around ions in crystal lattice. It interacts with electrons occupying the f shells, giving rise to magnetocrystalline anisotropy. Considering a case of single atom, CEF removes the directional degeneracy of nearby atoms. The splitting to multiplets also depends on the symmetry of CEF. The discrepancy between values of magnetic moments predicted by Hund's rules and experimental data is given by CEF. Hamiltonian of CEF can be calculated from first principles, using a general formula:

$$\hat{\mathcal{H}}_{\mathrm{CF}} = \sum_{L,M} B_L^M \hat{O}_L^M, \tag{2.16}$$

where B_L^M represents symmetry-dependent crystal field parameters and $\hat{O}_L^M$ are the so-called Stevens operators [30] representing the whole f shell.

In systems with $3d$ elements the CEF interaction ($\sim$ 1-2 eV in energy scale) quenches the orbital contribution to ionic magnetic moments [27] and spin-orbit interaction ($\sim$ 10 meV in energy scale) can be considered as a perturbation [31]. In the $4f$ systems the spin-orbit interaction ($\sim$ 100 meV) is responsible for the formation of terms whereas the CEF interaction ($\sim$ 10 meV) causes the splitting to multiplets [27].

Itinerant electron magnetism

Previous relations consider magnetic moments in an isolated atom or ion. However, embedding the ions into a metallic lattice, a contribution of conduction

electrons to the total magnetization has to be considered [27, 28, 31]. First attempt to describe metallic state was made by Pauli [32]. Each electron in a metal has a configuration of either spin-up or spin-down. Placed in a magnetic field, the energy of the electron will be increased/decreased depending on its spin. In other words, magnetic field splits the electron band into two sub-bands separated by $2\mu_{\mathrm{B}}B$ (see Figure 2.3). The magnetization is given by

$$M = \mu_{\mathrm{B}}(n_{\uparrow} - n_{\downarrow}) = g(E_{\mathrm{F}})\mu_{\mathrm{B}}^2 B, \tag{2.17}$$

where $n_{\uparrow}$ ($n_{\downarrow}$) is the number of spin-up (spin-down) electrons per unit volume and $g(E_F)$ is the density of states at the Fermi level [23]. It gives rise to the paramagnetic response of metals, called Pauli paramagnetism

$$\chi_{\mathrm{P}} = \frac{M}{H} = \mu_0 \mu_{\mathrm{B}}^2 g(E_{\mathrm{F}}). \tag{2.18}$$

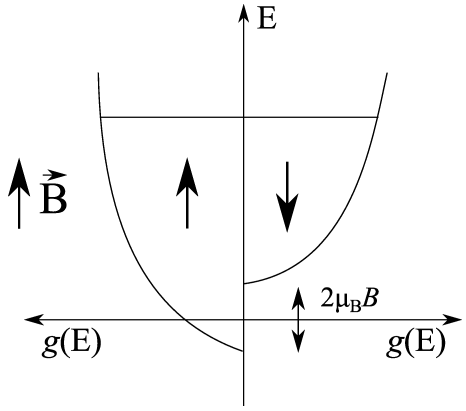

Figure 2.3: Density of states showing the splitting of electron bands in applied magnetic field.

After the development of electron band model by Bloch [33], Stoner [34] finalized this theory employing electronic band structure instead of discrete angular momentum levels. This model fundamentally differs from the previously mentioned localized one and it is based on the prominent spatial distribution of $3d$, $4d$, $5d$ transition metal and $5f$ light actinide wave functions (see Figure 2.2). Since these compounds lose their localized character they cannot be described using Hund's rules. First, we consider three simple ferromagnetic $3d$ metals Fe, Co and Ni.

	Fe	Co	Ni
M_{s} (μ_{B}/atom)	2.216	1.715	0.616
T_{c} (K)	1044 ± 2	1388 ± 2	627 ± 0.3

Table 2.1: Value of saturation magnetization M_{s} and Curie temperature T_{c} for Fe, Co and Ni [35].

The non-integer values of saturation magnetization M_{s} given in Table 2.1 cannot be obtained in the localized magnetism scenario. The reason for these

values is a different microscopic mechanism on the basis of spontaneous spin-splitting: let's suppose we move (without magnetic field) a small amount of electrons, in the energy range of δE, from spin-down band to spin-up band. The total energy change associated with such electron transfer is given by [23]

$$\Delta E = \frac{1}{2} g(E_{\mathrm{F}})(\delta E)^2 (1 - U g(E_{\mathrm{F}})), \tag{2.19}$$

where U scales the robustness of Coulomb interaction. From equation 2.19 we get a condition for spontaneous spin-splitting, i.e. case when the transfer of spins from one band to the other is energetically favourable

$$U g(E_{\mathrm{F}}) \geq 1. \tag{2.20}$$

Equation 2.20 is known as Stoner criterion [23, 36]. This condition for spontaneous ferromagnetic ordering requires strong Coulomb interaction and also large density of states at the Fermi energy. If the equation 2.20 is not satisfied ($U g(E_{\mathrm{F}}) < 1$), ferromagnetism will not occur. Nonetheless, the magnetic susceptibility of interacting free electron gas is changed

$$\chi_{\mathrm{S}} = \frac{\chi_{\mathrm{P}}}{1 - U g(E_{\mathrm{F}})}, \tag{2.21}$$

where χ_{P} represents the Pauli susceptibility introduced in equation 2.18 and the denominator is the Stoner enhancement factor. More advanced method for treating real systems is developed within the framework of density functional theory [37].

2.3 Interactions between magnetic moments

Exchange interactions are crucial for the emergence of long-range magnetic ordering. They represent electrostatic interactions between electrons arising from the antisymmetric nature of the overall wave function [23]. In the Heisenberg model, the spin-dependent Hamiltonian describing the energy of these interactions is written as

$$\hat{\mathcal{H}} = -\sum_{i,j} J_{ij} \mathbf{S}_i \cdot \mathbf{S}_j, \tag{2.22}$$

where J_{ij} is the exchange integral between i^{th} and j^{th} electron and $\mathbf{S}_i$, $\mathbf{S}_j$ are spin quantum numbers of i^{th} and j^{th} electron, respectively [27].

There are three basic types of interactions [27]:

Direct exchange occurs between neighbouring magnetic atoms, with sufficient overlap of their wave functions. The magnitude of exchange integral J_{ij} exceeds 10^2 - 10^3 K. The exchange proceeds without any intermediary and occurs in materials containing d-electrons (Fe, Co, Ni) or $5f$-electrons (uranium compounds). It is not effective in rare earth compounds due to the strongly localized character of the $4f$ wave functions.

Indirect exchange or superexchange describes the interaction between magnetic moments too far apart to be connected by direct exchange. The exchange

integral J_{ij} is reduced, comparing with the previous case, possessing a value around 10^0 - 10^2 K. In this case a non-magnetic intermediary ion provides the interaction. Superexchange can be found in materials containing d-electrons or $4f$-$5f$ intermetallic compounds with p- or d-electrons.

RKKY (Ruderman-Kittel-Kasuya-Yoshida) exchange named after its main proposers [38, 39, 40] is a long-range interaction between strongly localized $4f$-electrons where any direct interaction is excluded due to lacking overlap of wave functions. It has an oscillatory dependence on the distance r between magnetic moments and can be written as a r-dependent exchange interaction

$$J_{\mathrm{RKKY}} \propto \frac{\cos(2k_{\mathrm{f}}r)}{r^3}, \tag{2.23}$$

where we assume a spherical Fermi surface with radius k_{f}.

2.4 Types of magnetic order

In materials with strongly interacting magnetic moments cooperative phenomena can be observed when the exchange interaction energy exceeds the energy of the thermal movement of magnetic moments. These phenomena lead to a long-range periodic magnetic ordering below a critical temperature. Ferromagnetism and antiferromagnetism represent the basic types of magnetic ordering; except these configurations, more complex structures can be found, such as ferrimagnetism, helical order or spin-glass.

Ferromagnetism

A ferromagnetic material reveals a spontaneous magnetization even in the absence of applied magnetic field, i.e all magnetic moments are in parallel alignment. For a ferromagnetic material placed in a magnetic field $\mathbf{B}$, one should solve the Hamiltonian

$$\hat{\mathcal{H}} = -\sum_{i,j} J_{ij}\mathbf{S}_i \cdot \mathbf{S}_j + g\mu_{\mathrm{B}} \sum_j \mathbf{S}_j \cdot \mathbf{B}, \tag{2.24}$$

where the first term appeared already in the equation 2.22 and it is called the Heisenberg exchange Hamiltonian ($J_{ij} > 0$ for ferromagnets). The second term is the Zeeman term describing the interaction between applied magnetic field and magnetic moments in the material [23]. In order to solve equation 2.24, one should define a so-called effective molecular field or Weiss field $\mathbf{B}_{\mathrm{mf}}$, produced by the neighboring spins. This field measures the effect of magnetic ordering in the system. To parametrize the strength of the molecular field an empirical constant λ is used

$$\mathbf{B}_{\mathrm{mf}} = \lambda\mathbf{M}. \tag{2.25}$$

If we now apply magnetic field $\mathbf{B}_{\mathrm{e}}$, we can rewrite the paramagnetic susceptibility χ_{P} (equation 2.8) into

$$\chi_{\mathrm{P}} = \frac{\mu_0\mathbf{M}}{(\mathbf{B}_{\mathrm{e}} + \mathbf{B}_{\mathrm{mf}})} = \frac{C}{T}. \tag{2.26}$$

Considering a linear change of external magnetic field $\mathbf{B}_{\mathrm{e}}$, a physical quantity $\theta_{\mathrm{P}} = C\lambda$ called Weiss temperature can be introduced, and the magnetic susceptibility

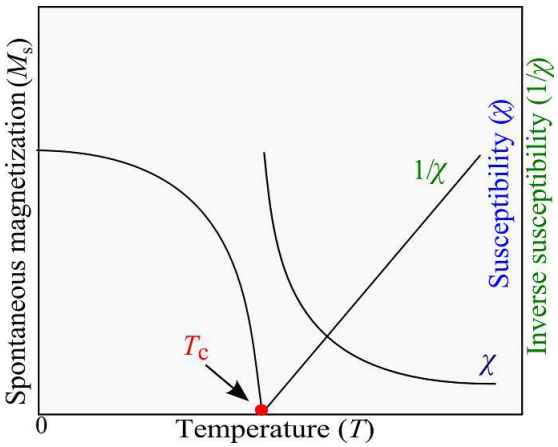

Figure 2.4: Temperature dependence of (inverse) magnetic susceptibility and spontaneous magnetization in a ferromagnetic material. T_C is the Curie temperature.

is given by

$$\chi = \frac{C}{T - C\lambda} = \frac{C}{T - \theta_P}. \tag{2.27}$$

Equation 2.27 represents the well-known Curie-Weiss law and describes the temperature dependence of a ferromagnet above the ordering temperature. For simple ferromagnets θ_P corresponds to T_C which is called the Curie temperature. A typical temperature dependence of spontaneous magnetization and (inverse) magnetic susceptibility is shown in figure 2.4. Common ferromagnetic materials include: iron (Fe), cobalt (Co), nickel (Ni) and gadolinium (Gd).

Antiferromagnetism

In an antiferromagnetic material ($J_{ij} < 0$ in Equation 2.22) we observe antiparallel alignment of adjacent magnetic moments (see Figure 2.5) below the ordering temperature T_N called the Néel temperature. Antiferromagnetism is often presented as a composition of two ferromagnetic sublattices oriented opposite to each other. To treat experimental data in the paramagnetic region one can define magnetic susceptibility as

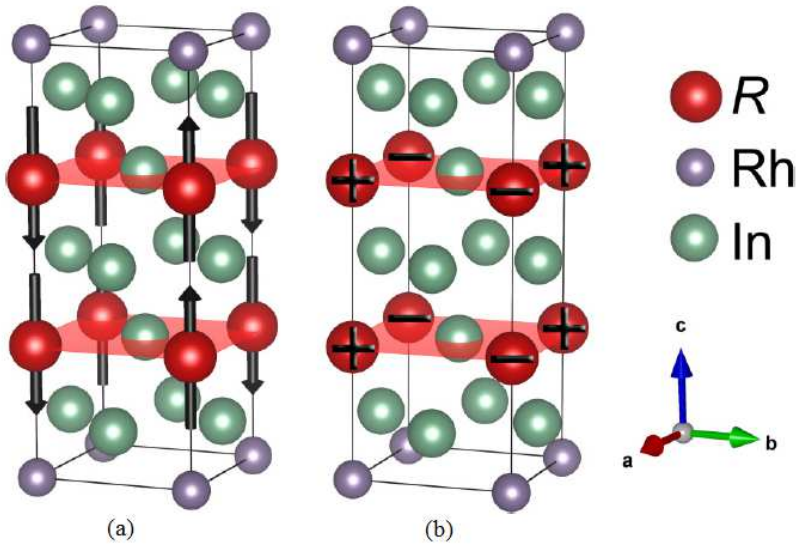

Figure 2.5: Magnetic structures of R_2RhIn_8 (R = Nd, Dy, Er) compounds. In the case of (Dy, Nd)$_2$RhIn$_8$ (a) a ++− stacking of magnetic moments is observed along the c-axis whereas in the case of Er_2RhIn_8 (b), the moments can point in any direction within the ab-plane but they have to be parallel to each other. Figure taken from [41].

$$\chi = \frac{2C}{T + T_N} \tag{2.28}$$

where C is the Curie constant from Equation 2.8. A typical temperature dependence of (inverse) magnetic susceptibility is shown in Figure 2.6. Examples of antiferromagnetic materials related to this work are: UIn_3, UGa_3, UPb_3 [14, 15, 16].

The temperature dependence of magnetic susceptibility for paramagnetic, ferromagnetic and antiferromagnetic materials can be generalized using Curie-Weiss law:

$$\chi \propto \frac{1}{T - \theta_P}, \tag{2.29}$$

where $\theta_P = 0$ is valid for a paramagnet; $\theta_P > 0$ points to a ferromagnet with T_C as the ordering temperature and $\theta_P < 0$ is characterized as an antiferromagnet with T_N as the ordering temperature.

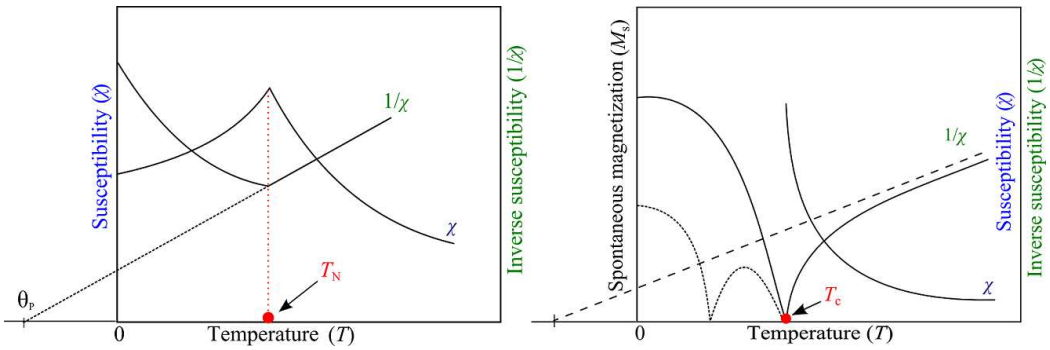

Figure 2.6: Temperature dependence of (inverse) magnetic susceptibility for an antiferromagnetic (left figure) and ferrimagnetic (right figure) material. T_N is the Néel temperature.

Ferrimagnetism can be viewed as an uncompensated antiferromagnet. Two magnetic sublattices with unequal magnetizations are aligned antiparallel to each other, they do not cancel out each other, therefore the total magnetization is non-zero (see Figure 2.6). With temperature variation we can achieve the magnetization to be zero at a characteristic temperature called the compensation temperature. Ferrimagnets usually do not show Curie-Weiss behavior. An example of uranium based ferrimagnetic compound is UAs [42].

Helical order or **helimagnetism** is typical for rare-earths metals, where the atoms tend to form layered structures. If there is a non-zero angle between magnetic moments lying in each layer, using nearest-neighbor and next-nearest-neighbor coupling a condition favoring helical order can be obtained. This magnetic order is energetically favourable than (anti-)ferromagnetism [23]. Representative compounds for such magnetic order is the $CeRhIn_5$ [7] (see Figure 2.7) which is iso-structural with $URhIn_5$, a compound thoroughly studied in this work.

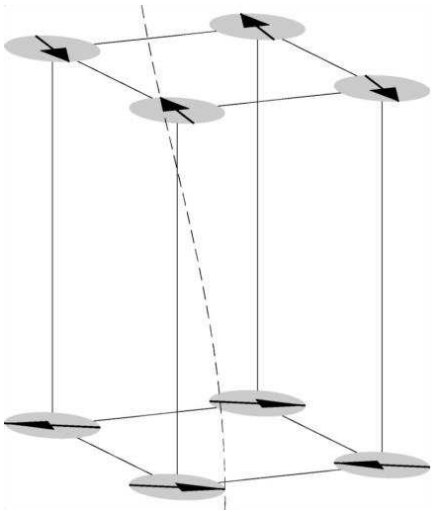

Figure 2.7: Magnetic structure of $CeRhIn_5$. The disk denotes the moment rotating plane. The dashed line traces the spiral. Taken from [7].

Spin glass behavior can be defined as a random magnetic system with mixed

interactions which is characterized by a freezing of spins at a well-defined temperature, called the freezing temperature. Below this temperature a metastable, short-range magnetic order appears. Typical example is CuMn alloy [43].

2.5 Strongly correlated electron systems

A wide range of magnetic systems can be described using simple models, i.e. mean field theory, described in the section about ferromagnetism. The basic assumption of this model is that electrons do not interact with each other but they are exposed to the effective field produced by surrounding spins. However in many cases such simple approach cannot be used. In systems with strong hybridization of inner d or f electrons and conduction electrons, correlations between electrons cannot be neglected. We call compounds showing similar features strongly correlated electron systems (SCES) [44]. These systems include high-temperature superconductors, cerium, ytterbium and uranium systems with Kondo interactions [45]. One of the main topics of SCES are compounds that exhibit heavy fermion behavior [46].

Heavy fermion compounds

Heavy fermion compounds (HF) have been a subject of intensive studies in the past several decades. $CeAl_3$ compound was the first representative of these systems [47]. This family of compounds is characterized by their anomalous specific heat behavior. At low temperatures the materials' heat capacity arises mainly from the contribution of conduction electrons. It is linearly proportional to temperature through the Sommerfeld coefficient. For simple metals the Sommerfeld coefficient γ is in order of units of mJ/mol·K^2 whereas in HF compounds this value can exceed 1000 mJ/mol·K^2. Since γ is proportional to the effective mass of the electrons, hence the name heavy fermions.

HF compounds are inherently close to quantum critical point (QCP) [48] and therefore suitable to investigate quantum criticality. The point at absolute zero temperature where matter becomes very sensitive to new forms of order is called the quantum critical point. At this point, no thermal fluctuations can occur, thus the phase transitions are driven by quantum fluctuations associated with Heisenberg's uncertainty principle [49]. The quantum critical behavior manifests itself by the occurrence of coexistence of magnetism and superconductivity ($CeRhIn_5$ [54]) and non-Fermi liquid (NFL) behavior [55]. NFL behavior deviates from Landau-Fermi liquid model [56] mainly in the temperature dependence of heat capacity, magnetic susceptibility and electrical resistivity. NFL is often observed in the vicinity quantum critical region where T_N goes to zero or the maximum of T_c is observed [57]. NFL behavior is interpreted in the framework of renormalization-group theory or self-consistent renormalization theory and solutions were proposed by several theoreticians [58, 59, 60, 61]. Critical behavior is also accompanied with the emergence of unconventional superconductivity ($CeCu_2Si_2$ [50]). Unconventional superconductivity cannot be described using the BCS (Bardeen-Cooper-Schrieffer) theory [51] as it excludes the coexistence of magnetically ordered moments with the classical s-wave superconducting Cooper pairs. In heavy fermion superconductors, cuprates and organic superconductors, the formation of superconducting state is described within a new approach

[52, 53]. In these materials it was suggested that the spin-spin interactions can substitute the role of phonons.

The very first strongly correlated electron systems included a single magnetic impurity ($3d$-metal) embedded in a metal host. This model is effectively described by the Anderson model [62]. In the limit of strong Coulomb interaction, the Anderson model reduces to the Kondo hamiltonian [45]. The characteristic temperature for the formation of ground state singlet within the Kondo model is given by

$$k_{\mathrm{B}}T_K = D\,\exp\left(-\frac{1}{JN(0)}\right), \tag{2.30}$$

where T_{K} is known as the Kondo temperature, $N(0)$ is the density of conduction electron states at the Fermi level and J is the coupling constant originating from exchange interactions. At $T = 0$ K, the ground state of the impurity spin is completely screened by the surrounding conduction electron spins with antiferromagnetic orientation, thus forming a non-magnetic state.

In a heavy fermion compound the $4f$ ions interact with each other and form the magnetically ordered state via spin polarization of conduction electrons, i.e. RKKY interaction (described earlier). The binding energy of this interaction is given by

$$k_{\mathrm{B}}T_{\mathrm{RKKY}} \propto J^2 N(0). \tag{2.31}$$

Thus, there are two competing mechanisms; the RKKY and the Kondo interaction. The competition of these interactions is schematically illustrated in the so-called Doniach diagram (see Figure 2.8) [63]. In the case of weak hybridization ($J \ll J_{\mathrm{c}}$) the RKKY interaction dominates and as a result the compound orders magnetically. On the other hand, with increasing hybridization the Kondo screening (formation of singlet state) becomes dominant. For $J \gg J_{\mathrm{c}}$ all the magnetic moments are fully screened, i.e. the compound is non-magnetic.

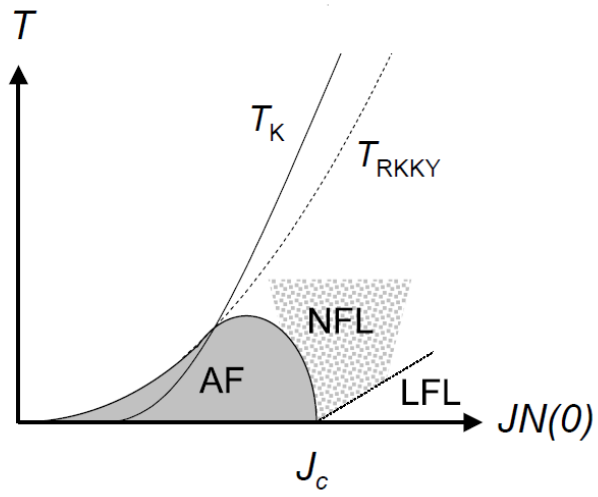

Figure 2.8: Schematic illustration of the competition between Kondo (T_{K}) and the RKKY (T_{RKKY}) interaction - Doniach phase diagram [63, 64]. The gray area represents the antiferromagnetically ordered state. Non-Fermi liquid behavior is observed near the critical value J_{c} where the QCP is located. For $J \gg J_{\mathrm{c}}$ Landau-Fermi liquid (LFL) is established. Figure taken from [65].

2.6 Magnetism in actinide intermetallics

The following section describes the ordering mechanisms in uranium and other actinide compounds and highlights differences between ordering mechanisms discussed earlier [23, 28]. As mentioned earlier, there are two basic types of magnetism in intermetallic compounds:

- Stoner magnetism is characteristic for $3d$ metals and it is connected with polarization of density of states at the Fermi energy.
- Localized magnetism is characteristic for $4f$ compounds. It is connected with the strong localization and weak interaction with surrounding environment of $4f$ wave functions responsible for magnetism. As a consequence of negligible mixing of $4f$ and conduction states the experimentally observed magnetic moments agree with the free ion value (with valence 3+) calculated from Hund's rules [27].

In general, actinide compounds can be considered as a transition between these two extreme conditions. Light actinides (up to Pu) are described by itinerant $5f$ electrons whereas heavier ones tend to have localized $5f$ electrons.

$5f$ states of uranium compounds

Uranium $5f$ wave functions are much more spatially extended compared to their $4f$ counterparts, therefore they perceive their physical and chemical surrounding more effectively (interaction between neighboring U atoms and with the metallic lattice). Consequently, uranium $5f$ states are delocalized due to their participation in bonding states along with a non-negligible hybridization

with non-U neighboring atoms in the crystal lattice [66]. This delocalized character is usually responsible for magnetism in uranium intermetallic compounds and has severe consequences:

- Experimentally observed magnetic moments are usually much smaller than expected ones for free U^{3+} or U^{4+} ions. Magnetic moments can disappear in the band limit resulting in Pauli paramagnetism described earlier. This behavior is similar to $3d$ metals.
- Compared to $4f$ compounds, where the RKKY interaction [39, 40] is dominant, the magnetic coupling is stronger in compounds containing $5f$ magnetic moments due to direct overlap of $5f$ wave functions.
- The high density of $5f$ states at the E_F is responsible for high γ values from low-temperature heat capacity and also for strongly anisotropic transport and magnetic properties.

Hybridization and $5f$-$5f$ overlap

Two types of microscopic mechanisms affect the $5f$ states; direct overlap of $5f$ wave functions of neighboring U atoms and $5f$-ligand hybridization.

In the first case the key parameter is the inter-uranium distance $d_{\text{U-U}}$. Compounds with small $d_{\text{U-U}}$ form a non-magnetic ground state (often superconductors) whereas large $d_{\text{U-U}}$ leads to magnetic ground state [67]. The critical limit, so-called Hill limit reaches values in the range $d_{\text{U-U}}$ = 0.34 - 0.36 nm. The presence of magnetic ground state is established by Stoner-type criterion. This simple rule neglects details of the density of states and $5f$-ligand hybridization leading to several exceptions with magnetic ordering with $d_{\text{U-U}}$ below Hill-limit (UNi_2 [68]) or non-magnetic compounds with $d_{\text{U-U}}$ above Hill-limit (URh_3 [69]).

The other important mechanism is the hybridization of $5f$ electrons and ligand valence states which is characteristic for compounds with $d_{\text{U-U}}$ well above the Hill limit. In case of strong hybridization this mechanism can be dominant leading to non-magnetic ground state in compounds with negligible overlap of $5f$ wave functions. When considering UX_3 (X = p-metal) compounds, the size of the p-atom is a crucial parameter [66]. In case of smaller X-ions (Si, Ge), the p wave function decays slower at the U-site, resulting in strong $5f$-p hybridization and lack of magnetic ordering (USi_3, UGe_3 [12, 13]) while larger X-ions cause the hybridization to be weaker, resulting in magnetic ground state (UIn_3, UPb_3 [14, 15]). In uranium compounds containing d-metals, the filling of d-states is also an important parameter that affects the strength of hybridization. Moving from left to right (increasing electronegativity) in transition metal series, the d-band is pushed further below E_F reducing the overlap of $5f$-d states and weakening the hybridization. Therefore, magnetism is observed with more electronegative d-metals in these compounds.

Magnetic moments in uranium compounds

The $5f$-band model offers a sufficient description for the majority of uranium intermetallic compounds. The appearance of uranium magnetic moments is based on spontaneous splitting of spin sub-bands resulting in total spin magnetic

moment μ_S. However, strong spin-orbit interaction in $5f$ systems induces large orbital magnetic moment μ_L, antiparallel to μ_S. Based on theoretical calculations, it was shown that the degree of delocalization of $5f$ states is reflected in the ratio of spin and orbital magnetic moment [70].

3. Experimental methods

3.1 Sample preparation

The very first step of every experiment in condensed matter research is the synthesis of samples. In our case, the preparation of novel, high-quality single crystals was crucial, thus we will go through the preparation in more detail.

Thermodynamics of crystal growth

From a thermodynamic point of view, compounds can be divided into congruently and incongruently melting ones. A congruently melting solid phase melts into a liquid phase with the same composition. On the other hand, incongruently melting solid phase melts into a liquid phase with different composition and another solid phase that has a different composition from the original solid.

Phase diagram is a temperature-composition scheme showing a possible coexistence of phases at the thermal equilibrium as a function of temperature. The phase diagram is a starting point of crystal growth preparation. Binary phase diagrams consist of two elements; in general n elements lead to N-dimensional phase diagrams. *Solidus-liquidus line* [71] is a boundary line between solid and liquid phases. At a peritectic point both solid and liquid phases transform into a solid phase. At the eutectic point the liquid phase transforms into two different solid phases.

The quality of the final crystals, either single or polycrystal, is largely dependent on the quality of the starting elements. The purity of the elements (metals) follows a rather simple notation: 4N5 = 99.995%, 5N = 99.999 %...etc. The uranium (U) used in our sample preparation was cleaned using Solid State Electrotransport (SSE) [72]. This technique uses ultrahigh vacuum and large DC current at high temperatures.

Single crystal preparation

Single crystal samples can be prepared by fundamentally different techniques: growth from melt, growth from vapor phase or growth from solution. Methods using growth from melt include: Czochralski method, Bridgman method and floating zone method [73, 74]:

- The *Czochralski method* or crystal pulling uses a seed crystal dipped into melt. After contact has been established between seed and the melted environment the seed is slowly rotated and lifted to obtain a single crystal.
- *Floating zone method* is advantageous for materials with high surface tension and low density. This method does not require any container but puts a limit on crystal diameter and length given by gravitational forces.
- During crystal growth using *Bridgman method* a steady motion of a freezing liquid-solid interface is utilized along an ingot. Either the whole ingot can be melted or a molten zone is established.
- Bulk single crystals can also be grown from *vapor phase* by sublimation,

chemical transport or chemical vapor deposition. These techniques are mainly used in silicon industry.

Since our samples were incongruently growing we used the only option to prepare them - the *flux method*. There are several advantages and disadvantages of this method:

- The most distinct advantage is the possibility to prepare incongruently growing compounds.
- During the growth process, crystals maintain their natural habitat.
- This method uses relatively simple equipment and consumes small amount of elements.
- The main disadvantage is that the stoichiometry cannot be controlled during growth which often leads to the presence of impurity phases.

The term "flux" describes a high temperature solvent that allows the growth to proceed at temperatures below the melting temperature of the solute phase. Self-flux method is usually used for compounds containing the solvent, whereas in the case of true-flux method the compound is grown from an additional element. The principle of the two methods is the same. Rather difficult part of the growth is the choice of the flux. Basic requirements of the flux include high solubility for the solute without the formation of unwanted binary phases. The melt should have a very low reactivity with the material of the crucible throughout the whole temperature range. Elements as Al, Ga, In, Sn or Pb are used as fluxes.

(a) (b) (c)

Figure 3.1: Necessary equipment for flux growth: (a) programmable furnaces with a temperature controller (b) the apparatus for sealing samples under vacuum or protective atmosphere (c) the laboratory centrifuge.

First, the non-stoichiometric composition of starting elements is prepared. This composition is usually different from the final product. Starting elements

are placed in a high purity (99.8 % or 99.99%) alumina (sintered Al_2O_3) crucible and sealed under vacuum (10^{-6} mbar) in a quartz tube (see Figure 3.2). The quartz ampules are than placed in a laboratory furnace and heated up to a temperature above the *solidus-liquidus line* of the desired composition. After a reasonable amount of time at the maximum temperature ($\sim$ 10 hours), dedicated to properly homogenize the melt, the cooling begins with a slow and constant rate ($\sim$ 3°C/h). The cooling rate affects the crystal sizes - the faster cooling the smaller crystals. When the temperature of the melt reaches the *solidus-liquidus line* [71], single crystals start to form and the solution becomes flux-richer due to the lever-rule [73]. Precise temperature controlling is essential for the stable growth of the crystals. In our case we used laboratory furnaces with built-in temperature controller with precision of ± 0.5 °C (see Figure 3.1).

Figure 3.2: Quartz ampules after centrifugation containing the crucibles with crystals and residual flux.

The growth must be stopped before reaching an eutectic point to avoid the formation of unwanted phases. The last step of the growth process is to decant the excess flux. This separation of solution from the crystals can be done mechanically, chemically or using a laboratory centrifuge (see Figure 3.1). The centrifugation is the most efficient way to separate the liquid solution from the crystals. The quartz ampules must be moved quickly from the furnace to the centrifuge to prevent the flux from solidifying. Chemical etching must dissolve the flux efficiently and on the other hand, it must not attack the crystals. In our case the remaining flux was etched by concentrated nitric acid (HNO_3) which does not attack the crystals. Mechanical removing of the crystals from the solidified flux is time consuming and disadvantageous due to the fragility of the crystals.

3.2 Structural and chemical characterization

3.2.1 *X*-ray diffraction methods

X-ray diffraction methods represent the crucial tool for structure, crystal quality (simple grain, twins...) and phase homogeneity (impurity) determination. Usually it is the first measurement which is performed after the crystal growth. *X*-rays

are produced in large scale facilities (synchrotron radiation) [75] as well as in small laboratories using X-ray tubes. The principle of X-ray diffraction is based on the constructive interference of wavelengths comparable with d_{hkl} (inter-planar distance of studied crystal lattice). This effect is observable only when Bragg's law is fulfilled [76, 77]:

$$2d_{hkl}\sin\theta = n\lambda, \tag{3.1}$$

where θ is Bragg's angle, n is the order of reflection and λ is the wavelength of the incident X-ray [76].

Laue method

Laue method is an experimental technique used to determine the quality and orientation of crystals. In this work we used back-reflection Laue method. A polychromatic wave emitted from X-ray tube is diffracted from a fixed sample.

Laue patterns were collected on a Photonic Science X-ray Laue System using a polychromatic Cu radiation. Diffraction patterns were collected with a CCD camera [78].

***X*-ray powder diffraction (XRPD)**

XRPD is a technique usually used for phase and structure characterization of both single and polycrystalline samples. Single crystals were powdered into fine powder and uniformly distributed on a silicon plate - in order to reduce the background. Diffraction patterns were taken on a Bruker D8 Advance diffractometer [79] equipped with a Cu lamp producing monochromatic Cu K_α radiation with wavelengths $K_{\alpha_1} = 1.540600$ Å and $K_{\alpha_2} = 1.544300$ Å. The diffractometer operates on the principle of Bragg-Brentano geometry [76]. The result of XRPD is a diffractogram, showing a 2θ dependence of intensity of diffracted beam.

For data treatment, structure determination FullProf/WinPlotr software was used [80, 81]. This software uses the Rietveld method [82] which evaluates the data on the basis of least square algorithm.

Single crystal *X*-ray diffraction

Measurements were performed both at the Department of Condensed Matter Physics (DCMP) [83] and at the Institute of Physics in the Czech Academy of Science (ASCR) [84].

Preliminary measurements of lattice parameters were performed at the DCMP on a RIGAKU RAPID II diffractometer [85] equipped with a molybdenium lamp (Mo) producing Mo K_α radiation and an image plate as a detector. The crystal structures were solved by CrystalClear software [86]. Crystal structures at the ASCR were determined using X-ray diffractometer Gemini, equipped with a molybdenum (Mo) lamp, graphite monochromator and an Mo-enhance collimator producing Mo K_α radiation, and a CCD detector Atlas. Absorption correction of the strongly absorbing samples ($\mu \sim 50$ mm^{-1}) was done by combination of the numerical absorption correction based on the crystal shapes and empirical absorption correction based on spherical harmonic functions, using the software of the diffractometer CrysAlis PRO. The crystal structures were solved by SUPERFLIP [87] and refined by software Jana2006 [88].

3.2.2 Scanning electron microscopy (SEM)

The results presented in this thesis were obtained using a Tescan Mira I LMH SEM [89], equipped with secondary electron (SE) and back-scattered electron (BSE) detector and with an energy dispersive X-ray analyzer (EDX) Bruker AXS [90]. SEM uses a focused, high energy (10-30 keV) electron beam to extract

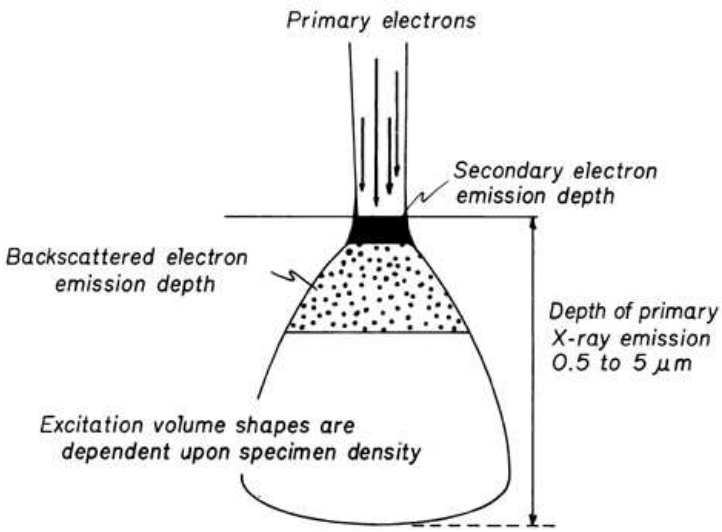

Figure 3.3: Bulk penetration of primary electrons. Picture taken from [91].

chemical or topographical information from a desirable region of the sample. High energy primary electrons, emitted by the electron gun, interact with the sample and a variety of signals is produced:

- Secondary electrons with energies < 50 eV originate from inelastic interactions between the primary beam and atoms near the sample surface. Therefore they provide mainly topographical information. This information is obtained from $\sim 1 - 10$ nm depth.

- Back-scattered electrons with energies > 50 eV are reflected out of the sample as a result of elastic scattering. They have worse spatial resolution than secondary electrons, but are more dependent on the atomic number Z, therefore they provide information about the distribution of different elements in the sample. Areas of the sample surface containing lighter elements appear darker, whereas areas with heavier elements appear lighter.

- Characteristic X-ray are primarily used to identify the chemical composition of the sample. Energy dispersive X-ray spectroscopy is based on the X-ray excitations of the sample. Every element has a unique electron shell structure; therefore interaction of high energy electrons with the sample produces a unique set of peaks on its spectrum [76]. EDX analysis also allows different types of scanning methods: point scan gives quantitative result from a small area given by the beam spot radius; line scan reveals information about the distribution of elements along specified line;

2D mapping gives qualitative information from the desired area revealing inhomogenities and impurity phases.

3.3 Physical Property Measurement System - PPMS

PPMS (see Figure 3.4) is a device, constructed by Quantum Design Inc., dedicated to measure a wide range of physical properties at extreme conditions. The accessible temperature range is between 1.8 - 400 K using ^{4}He; the system is also compatible with a ^{3}He insert that allows cooling down to 350 mK. Static magnetic field up to 9 T (14 T) induced in superconducting magnet is available in PPMS 9T (PPMS 14T) device. Detailed description of all possibilities is given in the device manual [92]. The measurements of electrical resistivity, ac susceptibility and specific heat down to 1.8 K can be also performed in hydrostatic pressures up to 3.2 GPa depending on the pressure cell type. In this work we measured mainly heat capacity and electrical resistivity, therefore we will focus on the description of these techniques.

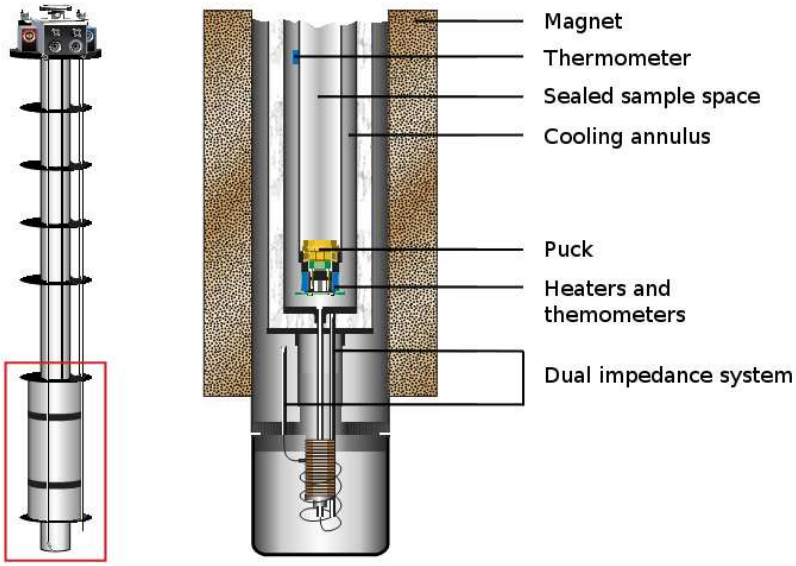

Figure 3.4: PPMS sample probe and a schematic cut of the system showing the sample space with measuring puck [92].

3.3.1 Specific heat

PPMS measures the heat capacity using two-tau (2τ) method. At the first stage of the measurement, the sample platform and puck temperatures are stabilized at some initial temperature. Then, power is applied to the sample platform heater, causing temperature rise. When the power is turned off, the temperature of the sample platform relaxes toward the puck temperature. In the two-tau model the first time constant (tau 1) is the relaxation time between sample platform and puck, and the second time constant (tau 2) is represents the relaxation between

the sample platform and the sample itself. The values of heat capacity are determined by optimizing the agreement between measured data and the two-tau model [93].

Heat capacity (specific heat), a thermodynamic quantity, is defined as an amount of heat necessary to change the temperature of (1 gram) a substance by 1 K

$$C_X(T) = (\frac{\delta Q}{\delta T})_X, \tag{3.2}$$

where X is a control (physical) parameter which is kept constant during the measurement. From the experimental point of view, the control parameter is usually pressure P. The temperature dependence of entropy can also be obtained from measurement of specific heat in a following way

$$C_P(T) = (\frac{\delta Q}{\delta T})_P = T(\frac{\delta S}{\delta T})_P \Rightarrow S(T) = \int \frac{C_P}{T} \mathrm{d}T \tag{3.3}$$

Since the entropy of the system $S(T)$ is directly related to energy levels due to thermal excitations, specific heat represents an effective macroscopic probe. $\mathrm{C}_P(T)$ is an additive thermodynamical quantity that can be written as a sum of individual contributions which become dominant in various temperature ranges:

$$C_P = C_{\mathrm{nuc}} + C_{\mathrm{el}} + C_{\mathrm{ph}} + C_{\mathrm{mag}} + C_{\mathrm{Sch}}, \tag{3.4}$$

where the terms represent nuclear, conduction electron, phonon, magnetic and Schottky contribution, respectively.

Nuclear contribution C_{nuc} is dominant at very low temperatures ($T<$ 0.5 K) where it is usually recognized by a $C_{\mathrm{nuc}} \sim T^{-2}$ dependence.

Conduction electron contribution C_{el} plays an important role up to temperature 4 K. Using the theory of free electron gas and Fermi-Dirac distribution, one can derive the exact form of C_{el} as

$$C_{\mathrm{el}} = \frac{1}{3}\pi^2 g(E_{\mathrm{F}}) k_{\mathrm{B}}^2 T = \gamma T, \tag{3.5}$$

where γ is the Sommerfeld coefficient which characterizes the proportionality of the electronic specific heat and temperature. Typical values of γ are in the $\mathrm{mJ{\cdot}mol^{-1}{\cdot}K^{-2}}$ range. Since the coefficient γ is proportional to the density of electronic states at the Fermi surface $g(E_{\mathrm{F}})$, it also gives information about the effective mass of electrons m_{e}. In heavy fermion materials the γ value becomes up to three orders of magnitude larger that one of a simple metal.

Phonon specific heat contribution C_{ph} is a consequence of lattice thermal vibrations represented by quasiparticles, called phonons. In a system with N atoms in a unit cell, phonons can be divided according to dispersion relations into $3N$-3 optical branches and 3 acoustic branches (see Figure 3.5). The optical branches can be described as a set of linear harmonic oscillators vibrating independently with a frequency ω_E, so-called Einstein frequency. The equation describing optical phonons in the Einstein model is as follows:

$$C_{\mathrm{ph}}^E = 3R \left(\frac{\Theta_E}{T}\right)^2 \frac{\exp(\frac{\Theta_E}{T})}{(\exp\frac{\Theta_E}{T} - 1)^2}, \tag{3.6}$$

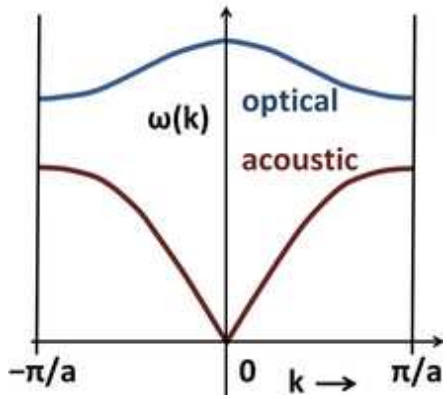

Figure 3.5: Scheme of phonon dispersion showing acoustical and optical phonons in a linear chain of two atoms. Figure taken from [94].

where $\Theta_E = \frac{\hbar\omega_E}{k_\mathrm{B}}$ is the Einstein temperature. This approach gives a reasonable agreement with experimental data at $T \to 0$ K and high temperatures. However, at low temperatures the Einstein model gives an exponential increase which is experimentally not observed.

With the assumption of distribution of different frequencies ω_D, the Debye model treats the acoustic phonons. Their behavior is described by the Debye integral

$$C_\mathrm{ph}^D = 9R\left(\frac{T}{\Theta_D}\right)^3 \int_0^{\frac{\Theta_D}{T}} \frac{\exp(x)}{(\exp(x)-1)^2} x^4 dx, \tag{3.7}$$

where $\Theta_D = \frac{\hbar\omega_D}{k_\mathrm{B}}$ is the Debye temperature and $x = \frac{\hbar\omega}{k_B T}$. This model gives better agreement with experimental data at low temperatures than the Einstein model. Phonon contribution at low temperatures can be described in a simplified way as

$$C_\mathrm{ph} = \beta T^3 \tag{3.8}$$

where $\beta = \frac{12}{5}\pi^4 R(\frac{1}{\theta_\mathrm{D}})^3$. The whole temperature range can be fitted with an empirical polynomial function appropriate for the Debye model in order to obtain an estimate of the Debye temperature [95].

$$C_\mathrm{ph}^D = \frac{24.9416 + 0.05313x_D^2 + 9.85\cdot 10^{-4}x_D^4 + 4.8\cdot 10^{-7}x_D^6}{1 + 0.0521x_D^2 + 8.71\cdot 10^{-4}x_D^4 + 4.56\cdot 10^{-6}x_D^6 + 2\cdot 10^{-8}x_D^8}, \tag{3.9}$$

where $x_D = \frac{\theta_D}{T}$.

A more sophisticated model, including the effect of anharmonicity, is described by C. A. Martin [96]. The overall phonon contribution including both the Debye and Einstein model with the correction for anharmonicity is given by

$$C_\mathrm{ph} = R\left(\frac{1}{1-\alpha_D T} C_\mathrm{ph}^D + \sum_{i=1}^{3n-3} \frac{1}{1-\alpha_{Ei}T} C_\mathrm{ph}^{Ei}\right), \tag{3.10}$$

where α_D and α_{Ei} are coefficients of anharmonic corrections for acoustic and optical phonons.

In the high-temperature region (around room temperature), the phonon contribution is independent on any material and leads to the classical Dulong-Petit law:

$$C_{\mathrm{ph}} = 3Nk_{\mathrm{B}}, \tag{3.11}$$

where $3N$ represents the 3 degrees of freedom of N atoms.

C_{mag} is a contribution to the total specific heat which is present only in magnetically ordered systems. Magnetic contribution is usually obtained by subtracting electron and phonon contributions from the experimentally measured specific heat C_{P}

$$C_{\mathrm{mag}} = C_{\mathrm{P}} - (C_{\mathrm{el}} + C_{\mathrm{ph}}). \tag{3.12}$$

The temperature dependencies of C_P of the magnetically ordered systems are given by the spin-wave theory and they depend mainly on the type of magnetic ordering and the dimensionality of the system [97]:

$$C_{\mathrm{mag}} = AT^{\frac{d}{m}}\exp(-\frac{\delta}{T}) \tag{3.13}$$

where d corresponds to the dimensionality of the magnetic order and $m = 1$ (2) for antiferromagnet (ferromagnet). The additional term $\exp(-\frac{\delta}{T})$ describes magnetic excitations across a gap δ in the magnon spectrum.

According to the phenomenological Landau theory, the transition from a paramagnetic to a magnetically ordered state is a 2^{nd}-order phase transition which has a discontinuity in the specific heat. On the other hand, a 1^{st}-order phase transition manifests itself with a discontinuity in the entropy. Typical example of such transitions are transition into a superconducting state or a structural transition.

In the paramagnetic regime, the magnetic contribution can be described somewhat easier. It is given by the Schottky paramagnetic contribution C_{Sch} which is connected with crystal field perturbation. The energy splitting caused by crystal field effects contributes to the specific heat and it is called the Schottky anomaly:

$$C_{\mathrm{Sch}} = \frac{R}{T^2}\left\{\frac{\sum_{i=0}^{n}\Delta_i^2\exp(-\frac{\Delta_i}{T})}{\sum_{i=0}^{n}\exp(-\frac{\Delta_i}{T})} - \left[\frac{\sum_{i=0}^{n}\Delta_i\exp(-\frac{\Delta_i}{T})}{\sum_{i=0}^{n}\exp(-\frac{\Delta_i}{T})}\right]^2\right\}, \tag{3.14}$$

where $n = 2J + 1$ is the number of energy levels, $\Delta_i = \frac{E_i}{k_{\mathrm{B}}T}$ is the energy of the i^{th} level.

In the high-temperature limit the magnetic entropy can be described as

$$S_{\mathrm{mag}} = R\ln(2J + 1). \tag{3.15}$$

In compounds with a doublet crystal field ground state we obtain the maximum theoretical value associated with magnetic transition

$$\Delta S = R\ln 2. \tag{3.16}$$

3.3.2 Electrical resistivity

Alternating current transport option is used on PPMS to determine the electrical resistivity of measured sample. The current is produced in a current source with a maximum of 2 A and precision of 0.02 μA. The frequency range of this source is 1 Hz - 1 kHz. The measurement of resistivity is done by using four-point method (see Figure 3.6). The golden/copper wires are used as electrical contacts, fixed to the sample by conducting silver paste. The typical values of resistance for high-quality contacts were between 2-5 Ω at room temperature. The outer wires are connected to the current source whereas the inner ones allow the measurement of voltage on the sample. The values of resistivity is obtained from the knowledge of the distance of inner wires and cross section of the sample perpendicular to current direction. In the case of small samples the calculation of resistivity can be effected with error up to 15 %.

Electrical resistivity, a bulk property, quantifies how strongly a material opposes the flow of electrical current. It is given by collisions of conduction electrons on (quasi-) particles. Assuming independent scattering mechanisms, we can describe electrical resistivity using Matthiessen's rule:

$$\rho_{\text{tot}} = \rho_0 + \rho_{\text{e-ph}} + \rho_{\text{mag}}, \tag{3.17}$$

where ρ_0 denotes residual resistivity, $\rho_{\text{e-ph}}$ is the term arising from scattering on lattice vibrations and ρ_{mag} is the spin-disorder term.

Residual resistivity ρ_0 arises from the presence of crystal defects (impurity atoms, dislocations). This term is temperature independent and very small compared to other terms, in case of non-magnetic, single phase sample.

The scattering of conduction electrons on phonons at low temperatures can be described using the Bloch-Grüneisen formula, derived in the framework of Debye model mentioned above:

$$\rho_{\text{e-ph}}(T) = 4R_{\Theta_D}\left(\frac{T}{\Theta_D}\right)^5 \int_0^{\frac{\Theta_D}{T}} \frac{x^5}{(\exp(x)-1)(1-\exp(-x))}dx, \tag{3.18}$$

where R_{Θ_D} includes fundamental constants and electron-phonon coupling constant which is proportional to the phonon part of the resistivity in the Debye model. For low temperatures $\rho_{\text{e-ph}}(T)$ presents a T^5 dependence, whereas at high temperatures it can be approximated as a linear function.

The third term in Equation 3.17 includes spin-dependent scattering phenomena. In magnetic systems this term has to be treated differently above and below the magnetic transition temperature. In the magnetically ordered state $\rho_{\text{mag}}(T)$ depends on the peculiarities of the ordering and dispersion on quasi-particles, called magnons. In a non-gapped dispersion relation for ferromagnetic (antiferromagnetic) magnons, the temperature dependence of ρ_{mag}, below the ordering temperature, shows T^2 (T^4) dependence. In the case of a presence of gap Δ in the dispersion relation, the electrical resistivity below magnetic ordering can be described [97, 98]:

$$\rho_{\text{mag}}(T) = AT^2 + DT(1+2\frac{T}{\Delta})\exp(-\frac{\Delta}{T}), \tag{3.19}$$

where A is the term arising from electron-electron scattering in Fermi liquid, D depends on the spin-disorder resistivity and electron-magnon coupling constant.

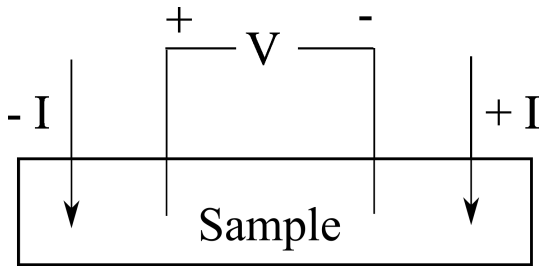

Figure 3.6: Scheme for the four-point method. Outer wires are connected to AC source and inner wires are used for measuring voltage on the sample.

To investigate the effect of hydrostatic pressure on the magnetic properties of studied samples, we measured the temperature dependence of electrical resistivity using a double-layered (CuBe/NiCrAl) piston-cylinder type pressure cell (see Figure 3.7) with Daphne 7373 oil as the pressure-transmitting medium [99, 100]. Pressures up to 3.2 GPa were reached.

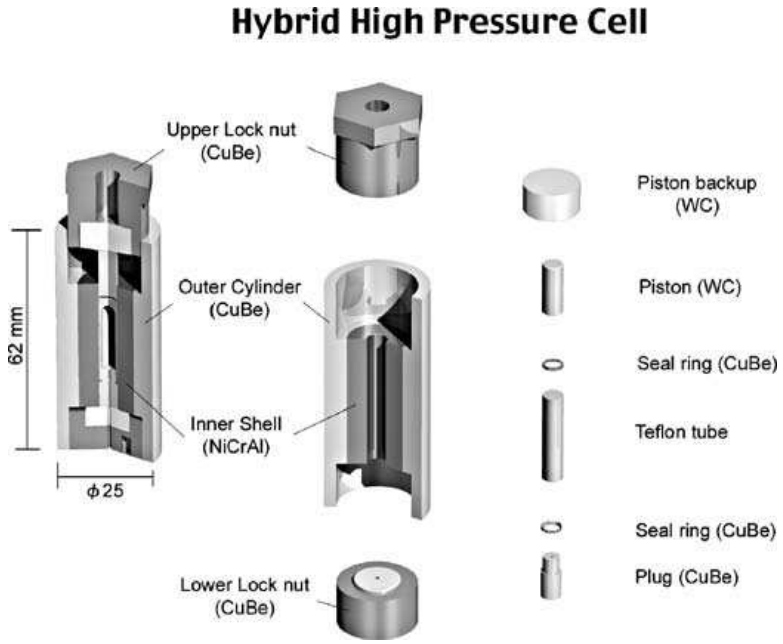

Figure 3.7: Cross-section view of a hybrid high pressure cell. Picture taken from [101].

The manganin wire (alloy of 86 % Cu, 12 % Mn and 2 % Ni) was used to determine the pressure inside the pressure cell. Pressure dependent resistivity of manganin is given by:

$$R(T,p) = R(T,0)(1 + \alpha(T)p) \tag{3.20}$$

where $\alpha(T)$ is the pressure coefficient of resistance of the manganin wire. At room temperature it takes the value of $\alpha(293\ \mathrm{K}) = 2.465{\cdot}10^{-3}$. The difference Δp between the room-temperature and the lowest measured temperature of the

Daphne 7373 oil inside the pressure cell is 0.3 GPa and remains constant throughout the range of used pressures. The real values of pressures inside the pressure cell were determined using linear pressure dependence of electrical resistivity of manganin wire at room temperature according to Equation 3.20 and the previously mentioned difference in pressure between room- and low-temperature.

3.4 Magnetic Property Measurement System - MPMS

The commercial magnetic property measurement system from Quantum Design Inc., is a magnetometer of SQUID (superconducting quantum interference device) construction. Its working principle is based on the Josephson junction [102]. The Josephson effect is a quantum mechanical phenomenon where electrical current flows without any applied voltage across the Josephson junction. The junction consists of two superconductors coupled by a thin insulating barrier. Cooper pairs [51] can flow through the barrier by means of quantum tunneling.

The SQUID determines the magnetic moment by measuring induced voltage while moving the sample through pickup coils. Two measurement options are available - extraction (DC method) or rapid oscillation by a servo motor (RSO - Reciprocating Sample Option).

The measured sample is fixed to a long thin rigid rod which is connected to a DC servo motor outside the sample chamber in the case of extraction. The SQUID technique is enormously precise and sensitive reaching the theoretical limit of $\sim 10^{-8}$ emu. The cryostat, in which the detection coils are placed, allows a wide temperature range between 1.8 K - 400 K and the application of external magnetic field up to 7 T.

3.5 Thermal expansion measurement

The measurement of thermal expansion is very complex and requires well-developed methods. There exists a wide range of non-contact methods based on optical measurements [103], X-ray [104] or neutron diffraction [105]. Other methods include mechanical contact with the sample: strain gauge [106], mechanical dilatometry [107] or capacitance method [108].

In this thesis we measured thermal expansion using capacitance method. We used a Vienna-type capacitance dilatometer [108] (see Figure 3.8).

The body of the cell is made of silver with the capacitor plates separated from each other by two brass needle bearings. These bearings with the sample are isolated from the silver body of the cell by sapphire discs [110]. The working principle is based on inverting construction [111]: sample expansion opens the capacitor and lowers its capacity, which is measured by a capacitance bridge. The temperature dependence of capacitance $C(T)$ is used to calculate the thermal expansion of the sample $\frac{\Delta l}{l}$.

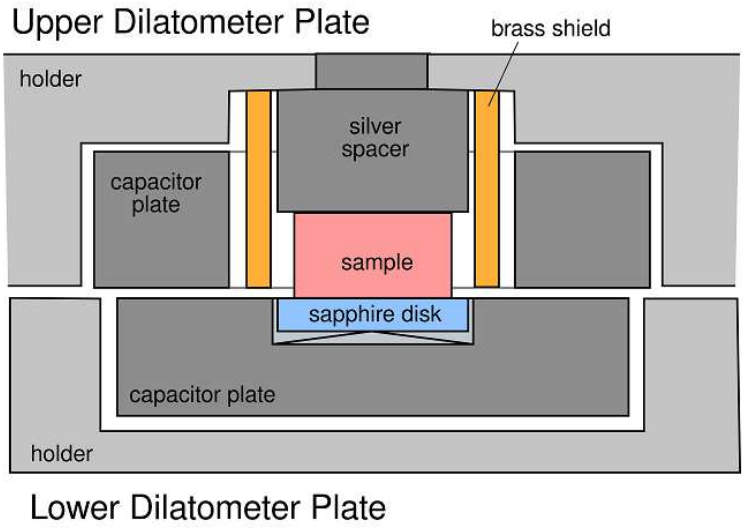

Figure 3.8: Cross section of capacitance dilatometer showing the position of the sample, capacitor plates, silver spacer and sapphire disk. Taken from [109].

3.6 Neutron diffraction

Neutron diffraction is a powerful experimental technique in solid state research that is based on the unique and convenient properties of neutrons:

- Neutron carries a zero electrical charge and thus, it has a large penetration depth in materials, typically in the order of centimetres.
- The wavelength of thermal neutrons is comparable to the interatomic distance in solids.
- Neutrons are scattered by the nuclei thus, they provide significantly better resolution of light elements and elements with similar atomic numbers than X-rays.
- Neutron possesses a non-zero spin ($S = \frac{1}{2}$). Consequently it allows the mapping of magnetic structures and excitations.

Neutrons can be produced by spallation or fission sources. Both techniques require large scale facilities.

Neutron scattering experiments can be divided into two groups, based on the energy of the neutron. If the energy of neutron remains unchanged before and after the scattering we talk about elastic scattering or diffraction. The other case, when the energy loss/gain of neutron measured, is called inelastic scattering. In this work we used neutron diffraction to determine the magnetic structure.

The intensity of the scattered beam is linearly proportional to the square of structure factor F_{hkl} is given by:

$$F_{hkl} = \sum_i b_c \exp(-iqr_i)\exp(-W_i), \tag{3.21}$$

where the sum is over the primitive cell, b_c is the coherent scattering length, q is the momentum transfer in reciprocal space, r_i is the position of the i^{th} atom and W_i represents the temperature factor.

The main difference between the X-ray and neutron diffraction is given by the scattering length b_c. While in X-ray scattering the cross section depends continuously on the number of electrons, for neutrons the cross section is arbitrary and it is unique for different isotopes of the chemical element [112]. This is the reason why it is difficult to distinguish neighboring atoms in the periodic table using X-ray scattering in contrast to neutron scattering.

In this work we used neutron diffraction for magnetic structure determination of $URhIn_5$ compound, therefore it is necessary to describe the magnetic scattering of neutrons. The contribution from magnetic scattering leads to additional diffraction pattern. The magnetic structure factor F_M is defined as:

$$F_M = p \sum_j f_j(q) m_j \exp(-iqr_i) \exp(-W_i), \tag{3.22}$$

where $p = 0.2692 \cdot 10^{-12}$ cm is a constant factor, f_j and m_j are the magnetic form factor and magnetic moment of the j^{th} atom, respectively [113].

PANDA - Cold three-axes spectrometer

PANDA (see Figure 3.9) is cold three-axis spectrometer located in FRM II Heinz-Maier-Leibnitz centre, Munich-Garching [114]. PANDA is used in solid state research for investigation of spin waves, crystal-field excitations, phonons and also for diffraction and inelastic scattering. Basic principles of three-axes spectrometry can be described using Figure 3.9. A polychromatic neutron beam (white beam) hits a single crystal monochromator (pyrolytic graphite (PG) (200) in the case of PANDA), which represents the first axis. Neutrons with defined wavelength are selected due to the Bragg law (Equation 3.1). After monochromization, the incident beam interacts with the sample, placed on the sample table. The orientation of the sample with respect to the incident beam can be changed by rotating the sample table i.e. the second axis. Neutrons may gain/lose energy by interacting with the sample and are detected with the detector placed behind the analyser crystal. On PANDA the detector is a 1D ^{3}He-tube and the analyser crystal is pyrolytic graphite. The desired energy can be selected by rotation of the analyser, on the same principle as for the monochromator. This is then the third axis of the instrument.

To determine the magnetic structure, we performed elastic neutron scattering which means that the incident (first axis) and the reflected (third axis) neutrons had same energy and it was kept constant during the experiment.

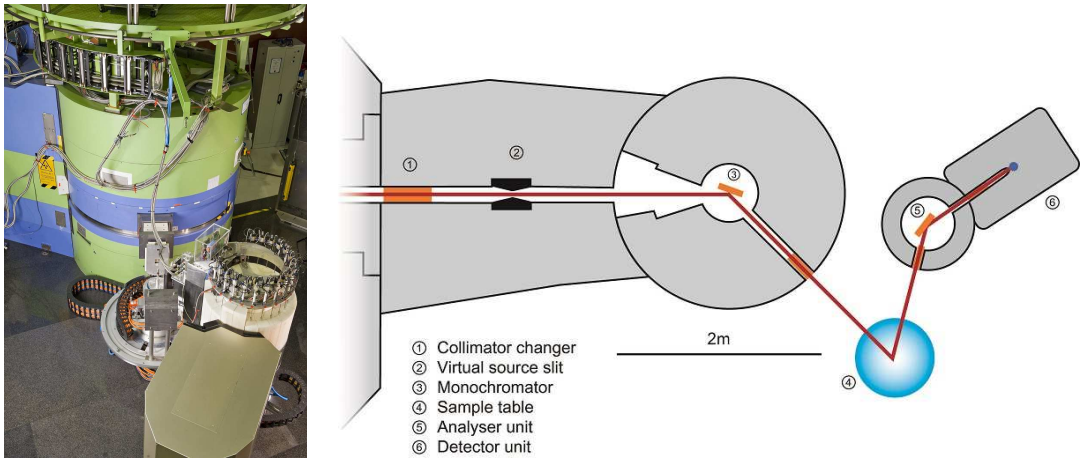

Figure 3.9: Real-life (left figure) and schematic (right figure) view of PANDA. Figures taken from [114].

3.7 Theoretical calculations

The method applied within this work is the density functional theory (DFT) within local density approximation (LDA) [116] and generalized gradient approximation (GGA) [117, 118]. For this purpose, two independent computational methods, namely the full potential augmented plane wave plus local orbitals method (APW-lo) and full potential local-orbital method (FPLO) were used to solve the single particle Kohn-Sham equations (for more details see [119]). Density functional theory is a quantum mechanical method used to investigate the electronic structure of many-body systems. DFT replaces the energy of an electron system with the electron probability density ρ. Its advantage is a little computational cost compared to other ab-initio calculations such as Hartree-Fock method. Classical DFT is based on solution of Kohn-Sham equations. Kohn-Sham potential takes into account electron exchange-correlation term. As we do not know this exchange-correlation potential of a general system exactly, we use approximate expressions instead. The most widely used approximation is LDA; the functional depends only on density at the coordinate where the functional is evaluated. GGA represents a numerical approximation which takes into account also the gradient of the density at the same coordinate.

The APW method solves Kohn-Sham equations not only close to nucleus but also in the interstitial region. The space of the unit cell is divided into spheres centered in each atom site and into the interstitial region. In the APW + lo method local orbitals (lo) are included to improve the APW basis.

4. Results and discussion

4.1 Synthesis

Single crystalline samples of UIn_3, $URhIn_5$ and U_2RhIn_8 were grown from In self-flux, using high purity elements (U – SSE, Rh – 3N5, In – 5N). The glass ampules with the batches placed in alumina crucibles were heated up (rate $\sim$ 200 °C/h) to the maximum temperature (950 °C in the case of U_2RhIn_8), kept there for 10 hours to let the mixture homogenize properly then cooled down (600 °C in the case of U_2RhIn_8) with a slow rate (3 °C/h) and decanted using a laboratory centrifuge ($\sim$ 2000 RPM). To optimize the size and quality of crystals we performed many (> 40) experiments using different starting compositions and temperature ranges. As a result of our growth process single crystals of typical dimensions of $1 \times 1 \times 0.5$ mm^3 were obtained. The temperature range for the growth of U_2RhIn_8 together with the growth products is shown in Figure 4.1.

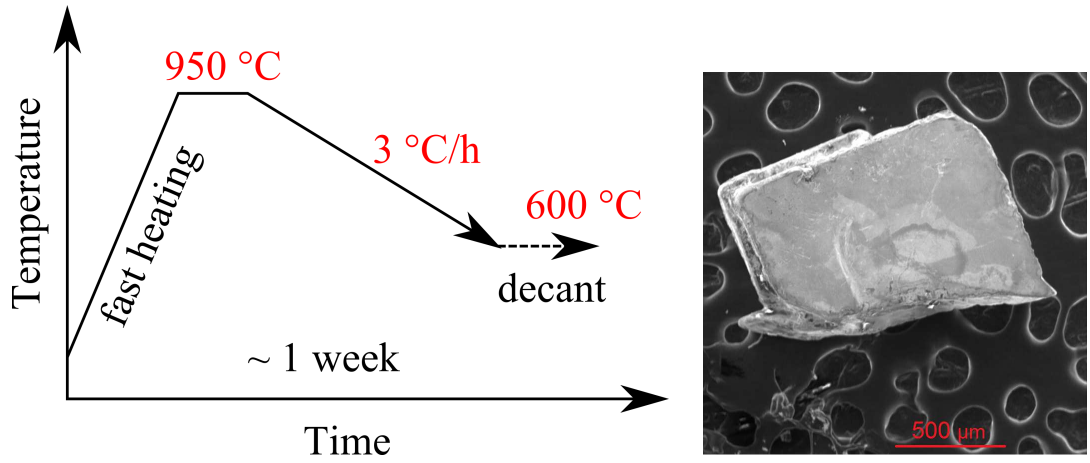

Figure 4.1: The temperature profile used for the successful growth of the U_2RhIn_8 single crystals. The $URhIn_5$ single crystal with typical dimensions is shown on the right-hand side.

Except the successful synthesis of $URhIn_5$ and U_2RhIn_8 we attempted the preparation of other compounds with the 1-1-5 and 2-1-8 stoichiometry with various transition and p-metals. Our efforts to prepare ternary compounds, from In self-flux with transition metals T = Mn, Fe, Co, Ni, Ru, Ir and Pt, resulted in the growth of UIn_3, binary phases such as $RhIn_3$, UIr, $RuIn_3$, Pd_3In_7 or UIrIn ternary alloy. As a result of Sn self-flux growth we obtained binary phases USn_3, $RhSn_2$ or $CoSn_2$. Single crystals of UIn_3 smaller than 50 $< \mu$m were obtained from starting stoichiometry 1:(5, 10, 15). The growth conditions for selected compounds are listed in Table 4.1.

T	U:T:In	T_1/T_2 (°C)	Final products
Mn	1:1:15	1100-400	UIn_3 ($\sim$ 1 mm), Mn-In binaries
Fe	1:1:15	1100-400	UIn_3 ($\sim$ 1 mm)
Fe	2:1:25	1100-400	UIn_3 ($\sim$ 1 mm)
Co	1:1:25	900-500	U-In and Co-In binaries
Co	2:1:25	900-500	U-In binaries
Ni	2:1:25	850-450	U-In binaries
Ru	1:1:25	900-500	U-In binaries
Ru	2:1:25	900-500	$RuIn_3$
Rh	1:1:25	950-600	$URhIn_5$, $U_4Rh_3In_{18}$ interphase
Rh	1:1:25	1050-750	$URhIn_5$, UIn_3 (<100 μm)
Rh	1:1:25	1100-550	$URhIn_5$
Rh	1:1:25	1050-750	$URhIn_5$
Rh	1:2:25	900-450	$RhIn_3$, UIn_3
Rh	2:1:25	950-600	U_2RhIn_8 (<100 μm)
Rh	2:1:25	1050-750	URhIn, $URhIn_3$
Rh	2:1:25	750-300	$RhIn_3$
Rh	2:1:25	900-500	U_2RhIn_8 (<150 μm), U-In binary
Rh	2:1:25	1100-400	$URhIn_5$, UIn_3
Rh	2:1:70	900-500	U_2RhIn_8
Pd	3:1:25	750-400	U_2PdIn_8, UIn_3 (<50 μm)
Pd	1:1:25	700-300	U-In binaries
Pd	2:1:25	700-300	U-In binaries
Pd	3:1:25	850-450	U-In binaries
Pd	2:1:25	850-450	U_2PdIn_8, UIn_3
Pd	2:1:25	1000-550	UIn_3
Ir	1:1:25	950-600	U-Ir binaries, UIrIn alloy
Pt	2:1:25	850-450	UIn_3 (<50 μm)
T	**U:T:Sn**	**T_1/T_2 (°C)**	**Final products**
Co	1:1:25	1100-650	USn_3, $CoSn_2$
Rh	1:1:25	1100-650	USn_3, $RhSn_2$
Ir	1:1:25	1100-650	UIrSn, U-Sn binaries
	U:In	**T_1/T_2 (°C)**	**Final products**
	1:5	800-500	UIn_3 (<50 μm)
	1:10	800-500	UIn_3 (<50 μm)
	1:15	800-500	UIn_3 (<50 μm)

Table 4.1: Growth conditions and final products of U_nTX_{3n+2} compounds. The starting (decanting) temperature is marked as T_1 (T_2). The largest dimension is stated in the columns.

4.2 Characterization

Energy dispersive X-ray analysis was performed on randomly selected single crystal to determine the precise chemical composition and homogeneity of the samples. Typical settings of measurements were 800-times magnification and 30 kV voltage on the electron gun. Results of point scans analyses with standard deviation provided by the ESPRIT software [79] are shown in Table 4.2.

UIn_3		U_2RhIn_8		$URhIn_5$	
U	27.9 ± 1.1	U	18.3 ± 0.8	U	15.7 ± 1.0
-	-	Rh	9.2 ± 0.3	Rh	13.7 ± 0.5
In	72.0 ± 1.6	In	72.6 ± 1.9	In	70.5 ± 1.9

Table 4.2: Energy dispersive X-ray analysis; point scan results with standard deviation.

For EDX analysis, samples were smoothly polished using diamond discs with grain sizes from 3 μm down to 0.1 μm. The point scans (see Table 4.2) revealed the composition of desired phases and the mapping scans confirmed the homogeneity of the samples.

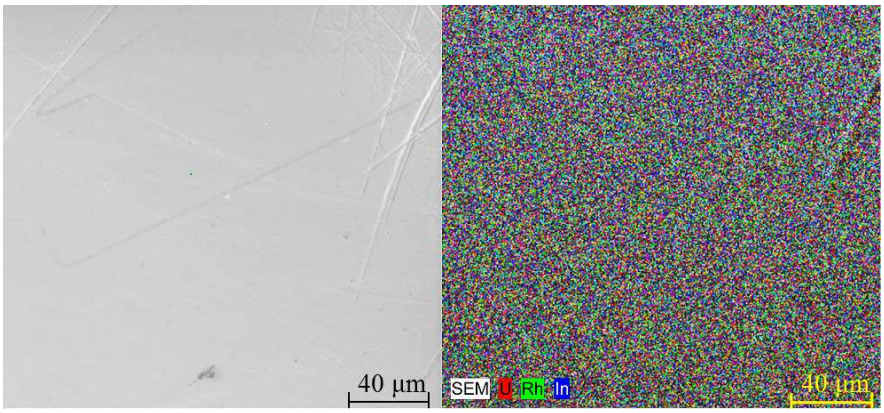

Figure 4.2: The left-hand side shows a polished area of a randomly selected U_2RhIn_8 sample in SE detector. The SEM mapping image is depicted on the right-hand side.

The 2D mapping scans for U_2RhIn_8 (see Figure 4.2) revealed the good homogeneity of the sample. In the case of UIn_3 the sample surface was contaminated with oxides. Mapping scan for $URhIn_5$ (not shown), also revealed good homogeneity of the sample.

To check the structure and phase purity of the samples, single crystal X-ray diffraction measurement was performed on U_2RhIn_8 and both single crystal and powder X-ray diffraction was measured on $URhIn_5$. Powder diffraction of U_2RhIn_8 was not measured due to small amount of crystals. The analysis of powder diffraction pattern of $URhIn_5$ (see Figure 4.3) confirmed the $HoCoGa_5$-type structure with space group P4/mmm (No. 123) and lattice parameters a = 4.6168(1) Å and c = 7.4145(1) Å. During Rietveld refinement of the powder diffraction pattern only the $URhIn_5$ phase was included. Every observed peak in the pattern can be described by the reflections from the $URhIn_5$ phase, except the one at $2\theta = 32.920°$ which arises from the (h k l) = (1 0 1) peak of pure indium (In).

Single crystal X-ray diffraction was performed on Rigaku Rapid instrument and on a Gemini X-ray diffractometer. The lattice parameters are listed an compared in Table 4.3. The atomic coordinates and Wyckoff positions obtained from single crystal X-ray diffraction on Gemini diffractometer are listed in Table 4.4

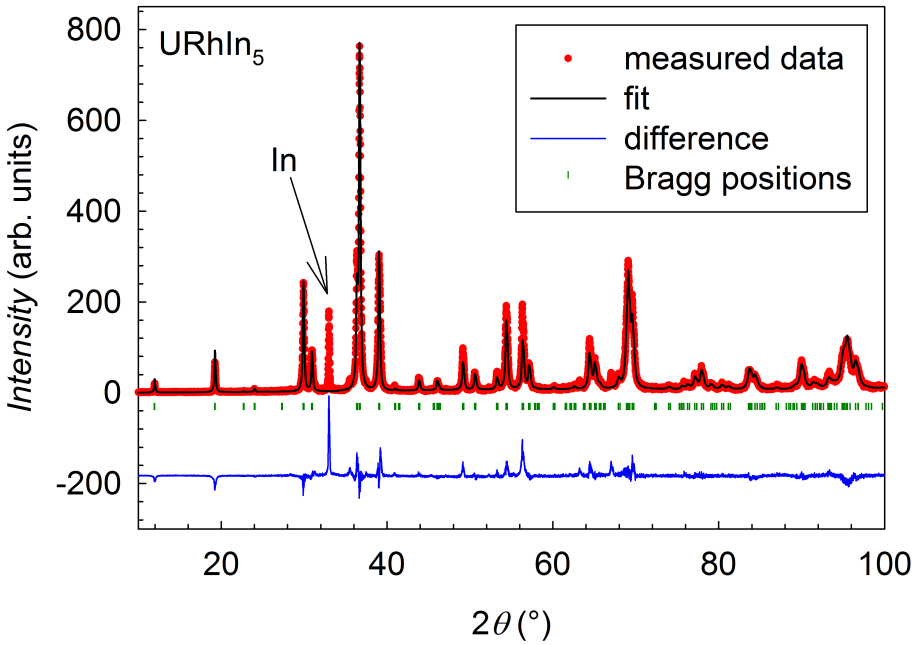

Figure 4.3: Powder X-ray diffraction pattern of $URhIn_5$. Vertical green lines show the Bragg positions of the $URhIn_5$ phase. Blue line depicts the difference between observed data (red points) and calculated fit (solid black line).

	Rigaku		Gemini	
Compound	a (Å)	c (Å)	a (Å)	c (Å)
$URhIn_5$	4.6159(2)	7.4120(6)	4.6210(5)	7.4231(7)
U_2RhIn_8	4.6163(6)	12.0144(4)	4.6077(6)	11.9911(15)

Table 4.3: Lattice parameters of $URhIn_5$ and U_2RhIn_8. Measurement results are compared from single crystal diffraction performed on Rigaku Rapid instrument [85] and single crystal X-ray diffraction performed on Gemini diffractometer.

Compound	Wyckoff position	x	y	z
$URhIn_5$				
U	$1a$	0	0	0
Rh	$1b$	0	0	0.5
In(1)	$4i$	0.5	0	0.30179(11)
In(2)	$1c$	0.5	0.5	0
U_2RhIn_8				
U	$2g$	0	0	0.30883(7)
Rh	$1a$	0	0	0
In(1)	$4i$	0	0.5	0.12263(11)
In(2)	$2h$	0.5	0.5	0.30916(14)
In(3)	$2e$	0	0.5	0.5

Table 4.4: Atomic coordinates and Wyckoff positions of $URhIn_5$ and U_2RhIn_8 obtained from single crystal X-ray diffraction.

Laue patterns were taken to verify the orientation and quality of single crystals. Laue pattern of $URhIn_5$ single crystal is shown on Figure 4.4 compared to calculated pattern using LauePt software [120].

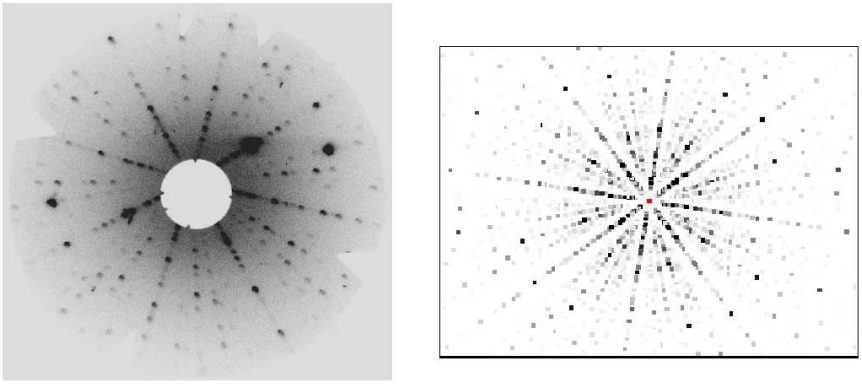

Figure 4.4: Laue pattern of $URhIn_5$ single crystal with its c-axis oriented perpendicular to the image plate is shown on the left-hand side. Calculated Laue patter using LauePt software [120] is shown on the right-hand side.

4.3 Physical properties

4.3.1 UIn_3

The UIn_3 compound forms the basic building 'block' of the layered tetragonal compounds studied within this thesis. We confirmed the magnetic properties measured previously [14, 18] and obtained a conclusive set of data.

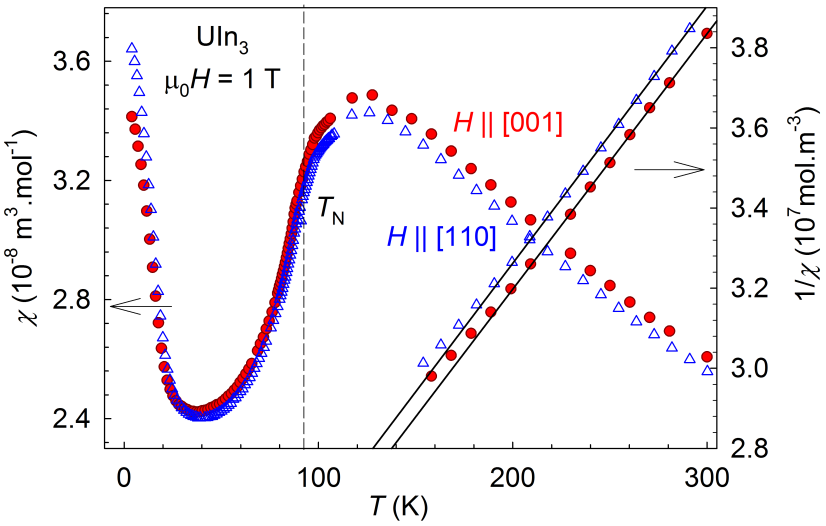

Figure 4.5: Temperature dependence of magnetic susceptibility and inverse magnetic susceptibility of UIn_3 in magnetic field $\mu_0 H = 1$ T oriented along [100] and [110] direction. Vertical dashed line shows the position of the Néel temperature obtained from the maximum of the $\partial(\chi T)/\partial T$ curve.

The temperature dependence of magnetic susceptibility and inverse magnetic susceptibility in magnetic field oriented along the [100] and [110] direction is shown on Figure 4.5. T_N was obtained as the maximum of the $\partial(\chi T)/\partial T$ curve [121]. The behavior of susceptibility and inverse susceptibility curves resembles the previously published data [14, 18]. First, the susceptibility increases with cooling; this increase and the shape of curves is similar in both [100] and [110] direction suggesting negligible magnetocrystalline anisotropy in this compound. The maximum value of magnetic susceptibility is reached at $T_{\chi_{max}} = 130$ K, consistently with literature [14]. A sharp decrease of $\chi(T)$ is observed in the vicinity of transition temperature $T_N = 88$ K reaching its minimum value at $T \sim 40$ K. At low temperatures the magnetic susceptibility shows an upturn and increases to the lowest measured temperature which is probably connected with impurities within the sample. Similar behavior was observed in the structurally related $CePd_3$ compound [123, 124]

The inverse magnetic susceptibility shows Curie-Weiss behavior above $T \sim 150$ K (see Figure 4.5). This linear temperature dependence was fitted according to Equation 2.8. The effective magnetic moments μ_{eff} and paramagnetic Curie temperatures θ_P are shown in Table 4.5. The disagreement between the published and our data probably arises from the different fitting interval, amount of impurities and/or size of the sample (diamagnetic contribution from the glue used to

fix the sample).

$\mathbf{UIn_3}$	μ_{eff} (μ_{B}/U)	θ_{P} (K)	μ_{eff} (μ_{B}/U) [14]	θ_{P} (K) [14]
$H \parallel$ [100]	3.16	-300	3.25	-176
$H \parallel$ [110]	3.15	-310	-	-

Table 4.5: Effective magnetic moments μ_{eff} and paramagnetic Curie temperatures θ_{P} from the Curie-Weiss fits. Results are compared to those published by Tokiwa *et. al.* [14].

4.3.2 $\mathbf{URhIn_5}$

$URhIn_5$ was prepared as the first ternary compound within the $U_n T In_{3n+2}$ family of compounds [1, 2]. In contrast to the cubic structure of UIn_3, it is more 2D-like, providing the possibility to investigate the 'dimensionality' effect on the $5f$ magnetism by means of magnetic susceptibility. Figure 4.6 shows the magnetic susceptibility of $URhIn_5$ in a magnetic field of 2 T oriented along the [100] and [001] directions. The temperature dependence of $\chi(T)$ shows a significant anisotropy where the [001] axis is the magnetic easy axis. The magnetic susceptibility starts to increases when cooling down from the room temperature. This increase is more pronounced in the [001] direction. The maximum value of $\chi(T)$ is reached at $T_{\chi_{\mathrm{max}}} = 160$ K consistently with literature [1]. The susceptibility shows a rapid decrease with decreasing temperature below $T_{\mathrm{N}} = 98$ K. This decrease is much more prominent for magnetic field in the [001] direction indicating that the ordered moments point to this direction in the ordered state. Recent nuclear quadrupole measurements support this speculation [122]. At $T \sim 50$ K, the susceptibility becomes almost temperature independent and starts to increase slightly again below $T \sim 10$ K. Noteworthy, the $\chi(T)$ curve for $H \parallel$ [100] differs significantly from published data [1]. The low-temperature increase of the susceptibility, as is seen in Figure 4.6 is much less pronounced in our data.

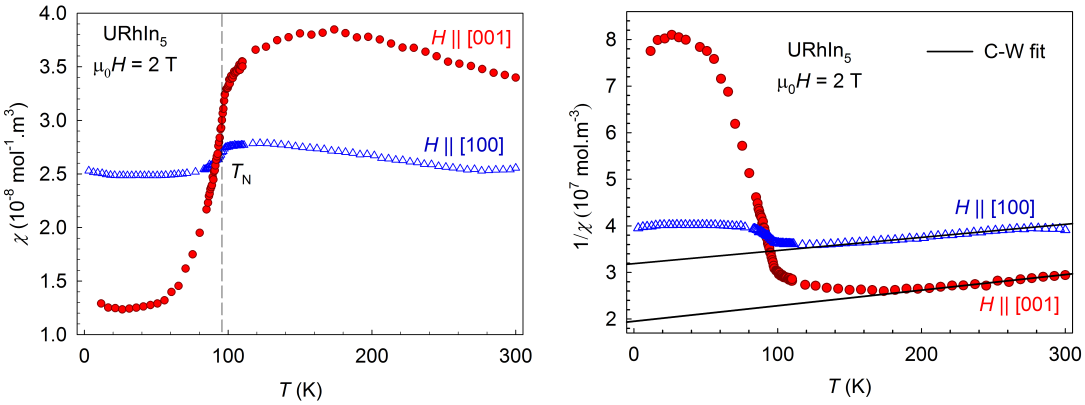

Figure 4.6: Temperature dependence of (inverse) magnetic susceptibility of $URhIn_5$ in magnetic field $\mu_0 H = 2$ T oriented along the [100] and [001] direction. Vertical dashed line shows the position of the Néel temperature obtained as the maximum of $\partial(\chi T)/\partial T$ curve. Solid lines represent the Curie-Weiss law fit.

This observation could point to an extrinsic nature of the upturn which means a smaller amount of impurities in our sample compared to [1] similarly to UIn_3 measurement.

The temperature dependence of inverse magnetic susceptibility is shown in Figure 4.6. From the character of the $1/\chi(T)$ curve above the Néel temperature it is evident, that the behavior of the $URhIn_5$ does not follow the Curie-Weiss law in the $H \parallel [100]$ direction. The linear behavior appears probably above 400 K as it was observed previously in $UPtGa_5$ [125]. We formally applied the Curie-Weiss law above 200 K to be able to compare our results with the previously published data [1]. Optimal fitting of the data resulted in an effective magnetic moment μ_{eff} = 3.71 μ_{B}/U, which is very close to the value of free U^{3+} ion (3.62 μ_{B}). Rather more striking are the large negative Curie-Weiss temperatures $\theta_{\mathrm{P}}^{[001]} = -500$ K for $H \parallel [001]$ and $\theta_{\mathrm{P}}^{[100]} = -900$ K for $H \parallel [100]$, indicating strong predominant antiferromagnetic spin exchange. The significant difference between the values $\theta_{\mathrm{P}}^{[001]}$ and $\theta_{\mathrm{P}}^{[100]}$ points to strong magnetocrystalline anisotropy in $URhIn_5$.

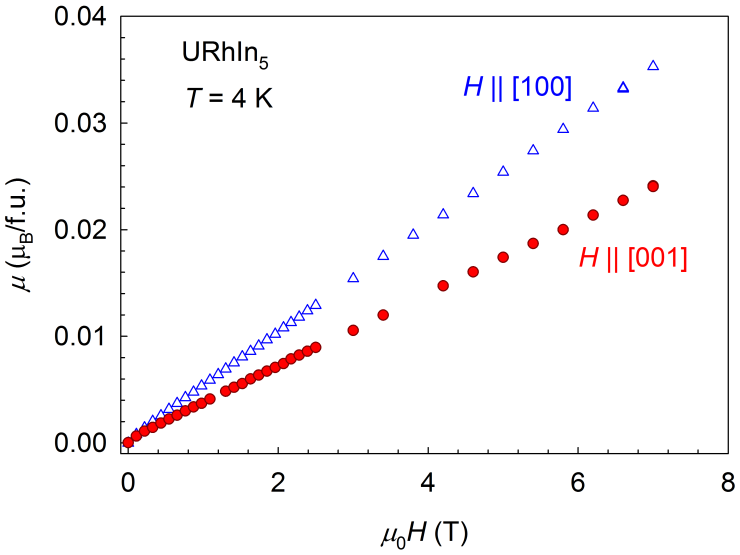

Figure 4.7: Magnetic field dependence of magnetization of $URhIn_5$ measured at 4 K in magnetic field oriented along the [100] and [001] axes.

The observed shallow maximum in $\chi(T)$ (see Figure 4.6) for $H \parallel [001]$ at $T \sim 160$ K is in agreement with that observed before [1] and discussed in context of a characteristic Kondo scale. When assuming that Kondo physics applies in $URhIn_5$ and neglecting crystal field influence, the Kondo temperature amounts to $T_{\mathrm{K}} = |\theta_{\mathrm{P}}|/4$ giving 125 K for $\theta_{\mathrm{P}}^{[001]}$ [126].

The magnetic field dependence of magnetization (see Figure 4.7) of $URhIn_5$ was measured at $T = 4$ K for magnetic field oriented along the [001] and [100] directions. Both magnetization curves reveal linear character up to 7 T. Using a relation $k_{\mathrm{B}} T_{\chi_{\mathrm{max}}} \simeq \mu_{\mathrm{B}} H_{\mathrm{c}}$ [127], where $T_{\chi_{\mathrm{max}}} = 160$ K defines the position of the maximum of the magnetic susceptibility data, and H_{c} is the critical magnetic field of metamagnetic transition, we obtain a value of $H_{\mathrm{c}} = 240$ T for $URhIn_5$. This extremely large value explains the absence of metamagnetic transition in our experimental data.

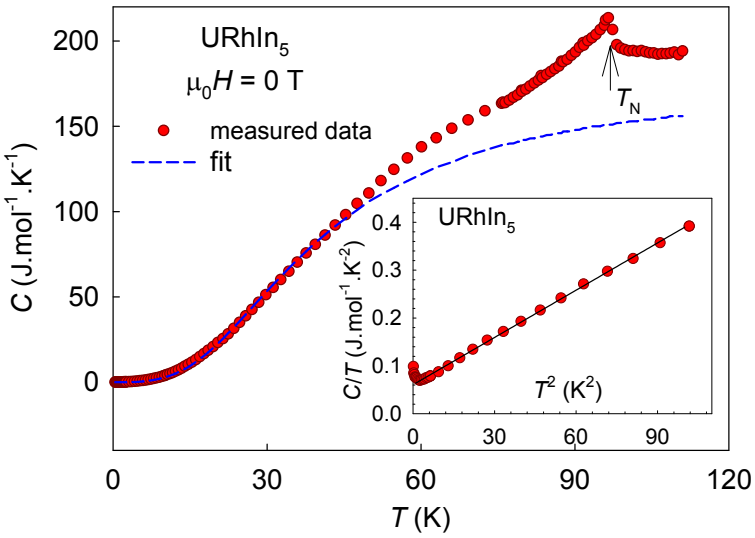

Figure 4.8: Temperature dependence of specific heat of $URhIn_5$. The transition into the antiferromagnetic state at $T_N = 98$ K is marked by an arrow. Dashed line shows the fit over the whole temperature range according to Equation 3.9. Inset: low-temperature part of the heat capacity with a $C/T = \gamma + \beta T^2$ fit.

Figure 4.8 shows the temperature dependence of specific heat $C(T)$ of $URhIn_5$. The clear λ-shaped anomaly at $T_N = 98$ K indicates a 2nd-order phase transition, consistently with literature [1]. However, contrary to those data, no additional feature in $C(T)$ at $T \sim 40$ K is observed showing very good quality of the single crystal. Since we do not have a non-magnetic analog to the $URhIn_5$, we can obtain only rough estimates of the contribution of conduction electrons and phonons. The magnitude for the contribution of conduction electrons was determined from a $C/T = \gamma + \beta T^2$ fit (see inset of Figure 4.8) to the data (fit interval 1 K $< T <$ 10 K). The value of Sommerfeld coefficient yields $\gamma = 60.7$ mJ·mol^{-1}·K^{-2} and the Debye temperature $\theta_D = 165$ K (see Figure 4.8) was obtained from fitting the whole temperature range with an empirical polynomial function appropriate for the Debye model (see Equation 3.9 [95]).

Figure 4.9 presents data in applied magnetic field of 9 T along the [001] direction. The direct comparison with the zero-field measurement reveals that the position of Néel temperature is almost unaffected within experimental uncertainty. Interestingly, the $CeRhIn_5$ counterpart is rather insensitive to the application of magnetic field along the same direction as well [7].

Figure 4.10 summarizes the overall temperature dependence of the electrical resistivity for current j applied along the [100], [110] and [001] axes. The room temperature resistivity equals 180 $\mu\Omega$cm in the basal plane and is only slightly lower for the c-axis direction $\rho^{[001]} = 170$ $\mu\Omega$cm. Noteworthy is the extremely high value of the residual resistivity ratio (RRR) exceeding 200 in the [100] direction. The RRR points to the high quality of the obtained single crystals. Note that the room temperature resistivity reaches almost the same value as reported by Matsumoto and co-workers [1]. Above T_N, the resistivity in all directions shows rather weak temperature dependence with positive "metallic" temperature coefficient $\mathrm{d}\rho/\mathrm{d}T$. The data manifest distinct anomalies with onset at around $\sim$

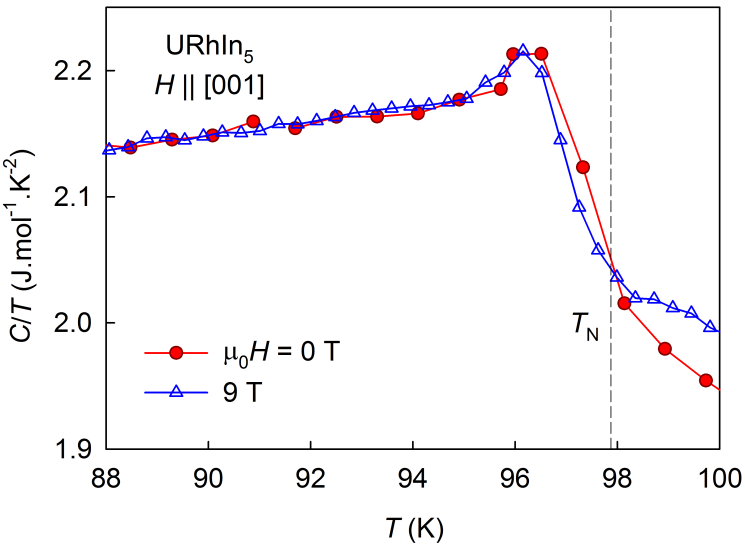

Figure 4.9: Comparison of heat capacity data in zero and 9 T magnetic field. Vertical dashed line shows the position of the transition temperature $T_N = 98$ K.

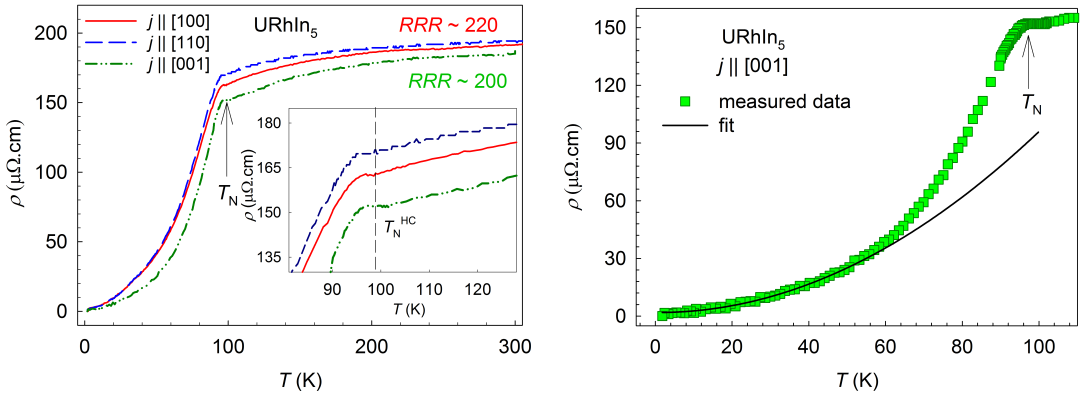

Figure 4.10: Temperature dependence of the electrical resistivity for current applied along the [100], [110] and [001] directions. The arrow marks the onset of the antiferromangetic phase transition. The inset shows the transition in more detail. Dashed line shows T_N obtained from the heat capacity measurements. Right figure shows the low-temperature fit of the electrical resistivity with current applied along the [001] direction.

100 K for $\rho^{[001]}$ and at a slightly lower temperature $T = 98$ K for $\rho^{[100]}$ and $\rho^{[110]}$, respectively. Accordingly, the onset marks T_N and the increase in resistivity results from opening of the SDW gap. Below T_N the resistivity in all directions drops rapidly. The temperature dependence of ρ down to lowest T can be fitted using the equation appropriate for an energy gap (Δ) antiferromagnet with an additional T^2 Fermi-liquid term (see Equation 3.19).

By optimal fitting of $\rho^{[100]}$ we obtain a residual resistivity value $\rho_0 = 1$ $\mu\Omega$cm, an electron-electron scattering coefficient $A = 0.013$ $\mu\Omega$cm·K^{-2}, an electron-magnon and spin-disorder scattering prefactor $D = 0.35$ $\mu\Omega$cm·K^{-1} and $\Delta = 82$ K. Our fit yielded similar values of the parameters for electrical current along the [110] direction. However in the case of $j \parallel [001]$ we obtained a somewhat

higher value of the gap energy $\Delta = 119$ K.

After evaluating the data from specific heat and electrical resistivity measurements of $URhIn_5$, the Kadowaki-Woods [128] ratio A/γ^2 could be calculated. Here, A is the coefficient of the quadratic term in the temperature dependence of electrical resistivity. The value of $3.6{\cdot}10^{-6}$ $\mu\Omega$cm·(mol·K/mJ)^2 was obtained for $URhIn_5$, being one order of magnitude lower than in the common heavy-fermion systems.

4.3.3 U_2RhIn_8

The U_2RhIn_8 compound represents the missing link, in the sense of structural dimensionality, between the purely cubic UIn_3 and the 2D-like $URhIn_5$. After the successful synthesis of this compound in single crystalline form we focused on the investigation of magnetic and transport properties.

The temperature dependence of specific heat $C(T)$ for U_2RhIn_8 is presented in Figure 4.11; a clear λ-shaped anomaly at $T_N = 117$ K indicates a 2nd-order phase transition. Closer observation of $C(T)$ versus T curve of U_2RhIn_8 reveals a small anomaly at $T \sim 100$ K, which probably arises from a tiny amount of $URhIn_5$ (we found no evidence from EDX measurements to support this statement). The magnitude of the conduction electron contribution to the heat capacity was determined from a $C/T = \gamma + \beta T^2$ fit to the data from temperature interval 1 K $< T <$ 10 K. Since we do not have a non-magnetic analog, the results of the fit are only rough estimates. For U_2RhIn_8, the value of the Sommerfeld coefficient yielded $\gamma = 47$ mJ·mol^{-1}·K^{-2} and the Debye temperature $\theta_D = 150$ K was obtained from fitting the whole temperature range with the empirical polynomial function shown before (see Equation 3.9).

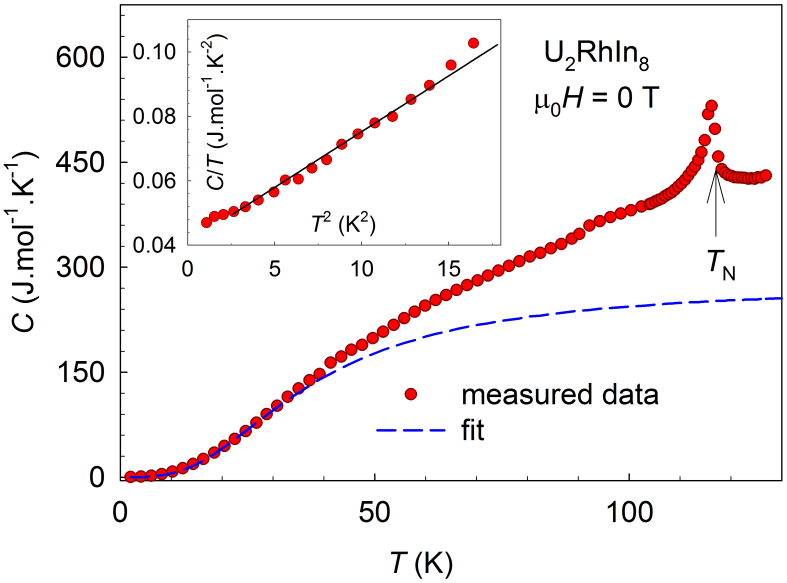

Figure 4.11: Temperature dependence of specific heat for U_2RhIn_8. The transition into the antiferromagnetic state is marked by an arrow at $T_N = 117$ K. Calculated value of heat capacity is marked with a dashed line. Inset: low-temperature part of the heat capacity with a fit to determine the magnitude for the contribution of conduction electrons.

Similarly to its more 2D-like counterpart, the transition temperature of U_2RhIn_8 is not affected by applied magnetic field up to 9 T (see Figure 4.12).

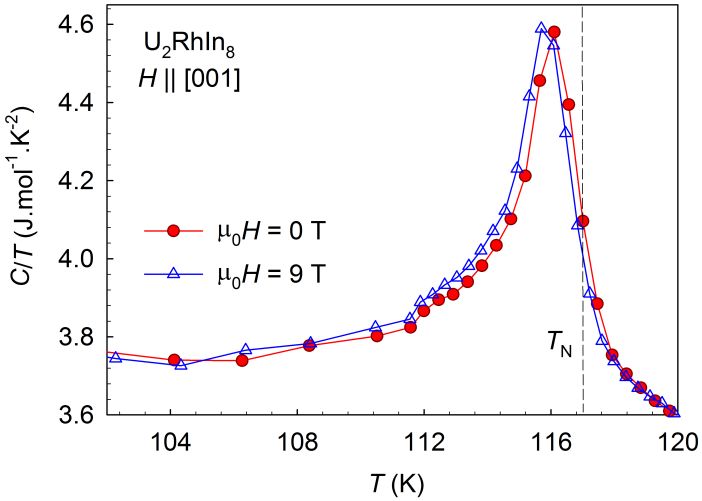

Figure 4.12: Comparison of the heat capacity data in zero and 9 T magnetic field applied along the [001] direction. Vertical dashed line shows the position of the transition temperature $T_N = 117$ K.

Figure 4.13 shows the magnetic susceptibility of U_2RhIn_8 measured up to 400 K in a magnetic field of 1 T oriented along the [100] and [001] directions. The temperature dependence of $\chi(T)$ shows a significant anisotropy similarly to its '115' counterpart. The Néel temperature was determined as the maximum of the $\partial(\chi(T))/\partial T$ curve [121]. The behavior of the susceptibility curves resembles the one shown for $URhIn_5$. The magnetic susceptibility increases with decreasing

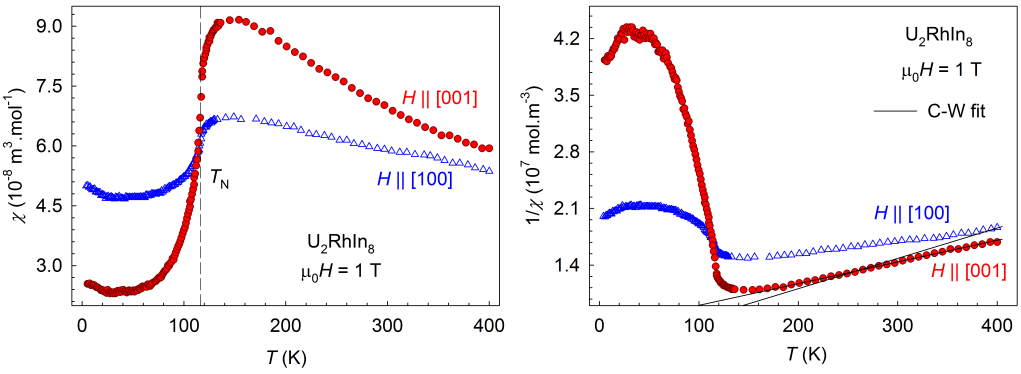

Figure 4.13: Temperature dependence of (inverse) magnetic susceptibility of U_2RhIn_8 in magnetic field $\mu_0 H = 1$ T oriented along the [100] and [001] direction. Vertical dashed line shows the position of the Néel temperature obtained as the maximum of $\partial(\chi T)/\partial T$ curve. Solid lines represent the Curie-Weiss law fit.

temperature up to 150 K, where the maximum of the $\chi(T)$ curve is reached. This increase is more pronounced in the [001] direction. The susceptibility shows

a rapid decrease with decreasing temperature below $T_N = 117$ K. This decrease is much more prominent for magnetic field in the [001] direction indicating that the ordered moments point to this direction.

The temperature dependence of inverse magnetic susceptibility is shown in Figure 4.13. From the character of the $1/\chi(T)$ curves above the Néel temperature it is evident that the behavior of U_2RhIn_8 does not follow the Curie-Weiss law in the $H \parallel [100]$ direction. The linear behavior of $1/\chi(T)$ in the [001] direction was observed above 350 K (see Figure 4.13) similarly to the structurally related $UPtGa_5$ compound [125]. Such recovery of Curie-Weiss law at high temperatures indicates a localized nature of $5f$ electrons. Thus, a crossover of the $5f$ electrons from a low-temperature itinerant nature to a high-temperature localized one is observed. This crossover effect is characteristic for many heavy-fermion compounds such as UPt_3, UPd_2Al_3 and URu_2Si_2 [125].

In accordance with previous arguments, we applied the Curie-Weiss law in the $H \parallel [001]$ direction. We obtained an effective magnetic moment of $\mu_{\text{eff}} = 3.45$ μ_B/U which is close to the value of free U^{3+} ion (3.62 μ_B). The large negative value of paramagnetic Curie temperature θ_P = -230 K reflects the huge magnetocrystalline anisotropy in U_2RhIn_8 induced by anisotropic $5f$-ligand hybridization. The Curie-Weiss law fit in the $H \parallel [100]$ direction results in an effective magnetic moment $\mu_{\text{eff}} = 3.62$ μ_B/U and a paramagnetic Curie temperature θ_P = -370 K.

Applying similar approach in the calculation of Kondo-temperature $T_K = |\theta_P|/4$, as in $URhIn_5$, we obtain $T_K = 57.5$ K for $\theta_P^{[001]}$ [126].

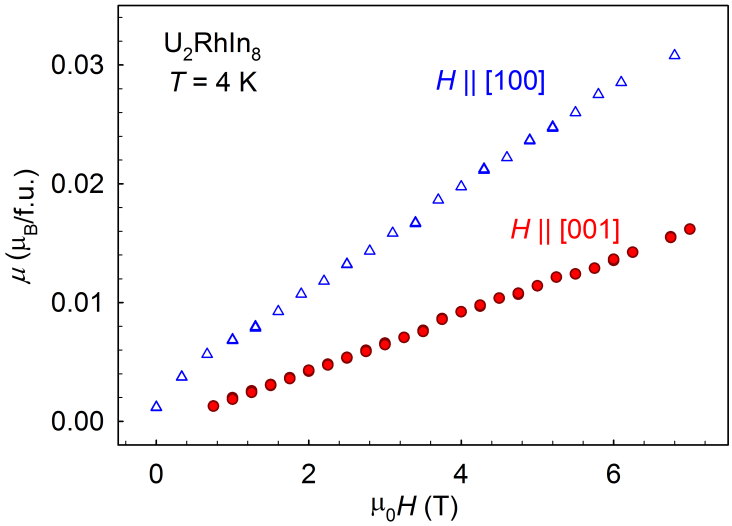

Figure 4.14: Magnetic field dependence of magnetization of U_2RhIn_8 measured at 4 K in magnetic field oriented along the [100] and [001] axes.

The magnetic field dependence of magnetization (see Figure 4.14) was measured at $T = 4$ K for magnetic field oriented along the [001] and [100] directions. Both magnetization curves reveal linear character up to 7 T; the [100] axis is almost twice higher than the magnetization in the other direction, which resembles the behavior of its more 2D counterpart [2]. On the other hand, it differs from the results published by Matsumoto *et al.* [1]. Using a relation $k_B T_{\chi_{max}} \simeq \mu_B H_c$

[127], where $T_{\chi_{max}} = 150$ K corresponds to the maximum in the magnetic susceptibility data, and H_c is the critical magnetic field of metamagnetic transition, we obtain a value of $H_c = 220$ T for U_2RhIn_8. This extremely large value explains the absence of metamagnetic transition in our experimental data.

Figure 4.15 shows the temperature dependence of the electrical resistivity of U_2RhIn_8 for electrical current j applied along the [100] and [110] axes. The room temperature resistivity equals 320 $\mu\Omega$·cm along the [100] direction and is only slightly lower for the [110] direction (310 $\mu\Omega$·cm). The residual resistivity ratio (RRR) exceeds 500 being a sign of a sample of very high quality. The electrical resistivity shows a monotonous decrease down to the value of the transition temperature T_N. Near the transition temperature $T_N = 117$ K, a tiny kink is observed, accompanied by a second-order phase transition and a formation of a gap at the Fermi surface. Subsequently, the resistivity decreases rapidly with decreasing temperature. The low-temperature part of the electrical resistivity (see Figure 4.15) can be fitted well using the equation appropriate for and energy gap antiferromagnet (Equation 3.19) [97]. In the interval 2 K $< T <$ 30 K best fitting of $\rho^{[100]}$ we obtain a residual resistivity value $\rho_0 = 0.56$ $\mu\Omega$cm, an electron-electron scattering coefficient $A = 0.006$ $\mu\Omega$cm·K^{-2}, an electron-magnon and spin-disorder scattering prefactor $D = 1.1$ $\mu\Omega$cm·K^{-1} and the energy gap $\Delta = 118$ K. Our fit yielded similar values of the parameters for electrical current along the [110] direction.

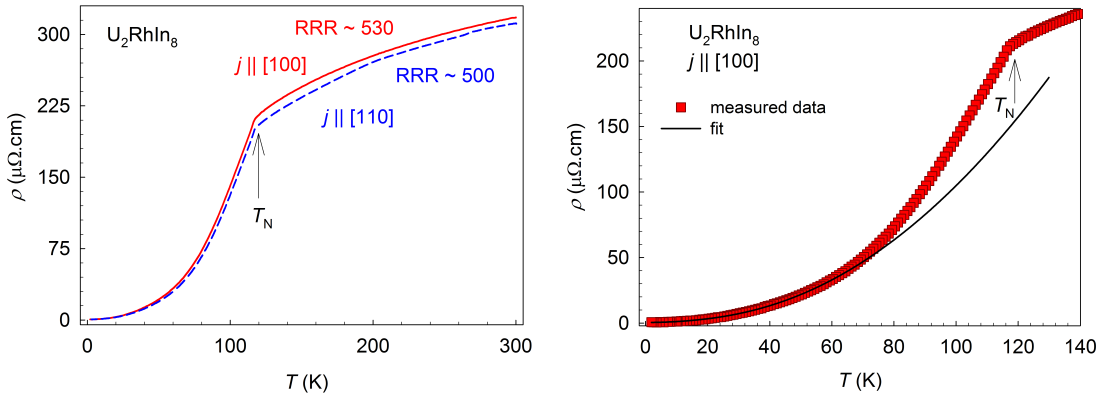

Figure 4.15: Temperature dependence of the electrical resistivity for current applied along the [100] and [110] directions. Arrow marks the position of the transition temperature T_N. Right figure shows the low-temperature fit of the electrical resistivity with current applied along the [100] direction.

After evaluating the data from specific heat and electrical resistivity measurements of U_2RhIn_8, the Kadowaki-Woods [128] ratio A/γ^2 could be calculated. The value of $2{\cdot}10^{-6}$ $\mu\Omega$cm·(mol·K/mJ)^2 was obtained for U_2RhIn_8. The Kadowaki-Woods ratio for U_2RhIn_8 and $URhIn_5$ is one order of magnitude lower than in the common heavy-fermion systems.

In order to investigate the effect of hydrostatic pressure on the transition temperature T_N, we measured the temperature dependence of electrical resistivity using a double-layered (CuBe/NiCrAl) piston-cylinder type pressure cell with Daphne 7373 oil as a pressure transmitting medium. Pressures up to 3.2 GPa were reached.

The temperature dependence of electrical resistivity for electrical current applied along the [100] direction under applied hydrostatic pressure is shown in Figure 4.16. The transition temperature T_N gradually increases with increasing pressure from 117 K at ambient pressure up to 126 K at 3.2 GPa with the rate of 5.4 ± 0.9 K·GPa^{-1}. This slope corresponds well to the pressure evolution of T_N in $URhIn_5$ [1] and UIn_3 [14].

The temperature-pressure phase diagram for U_2RhIn_8 is shown in Figure 4.16. The gradual increase of T_N can be explained using spin-fluctuation theory of an itinerant $5f$ electron system alongside with the Hubbard model [129, 130]. According to this scenario, hydrostatic pressure induces an increase in the hybridization between $5f$ and conduction electrons, which strengthens the exchange coupling J between U ions. On the other hand, it also decreases the $5f$ magnetic moment at the uranium site.

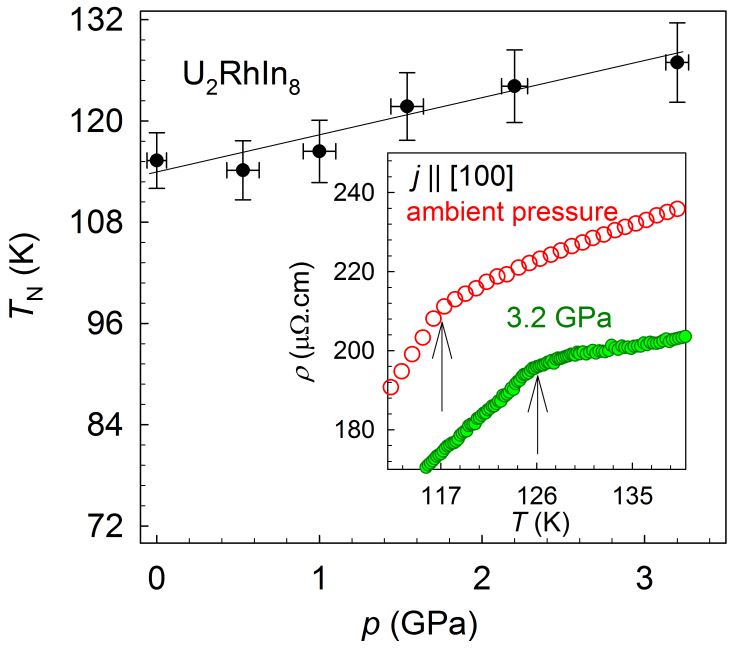

Figure 4.16: Temperature-pressure phase diagram of U_2RhIn_8. Inset shows the temperature dependence of the electrical resistivity for electrical current applied along the [100] direction at ambient pressure and at 3.2 GPa. Arrows indicate the transition at T_N.

The pressure evolution of T_N for U_2RhIn_8 is comparable to those of UIn_3 [14] and $URhIn_5$ [1] as is shown in Figure 4.17.

In order to acquire information about the temperature dependence of lattice parameters for U_2RhIn_8, dilatometry has been measured using a Vienna-type capacitance cell for thermal expansion in the PPMS 14T apparatus. The dimensions ($1 \times 1 \times 0.3$ mm^3) of selected single crystals allowed the measurement of thermal expansion only along the [001] direction.

The measurements were performed in zero magnetic field and the heating/cooling sequence with a rate of 0.1 K/min was repeated several times to confirm that the obtained results are reproducible. The results of thermal expansion

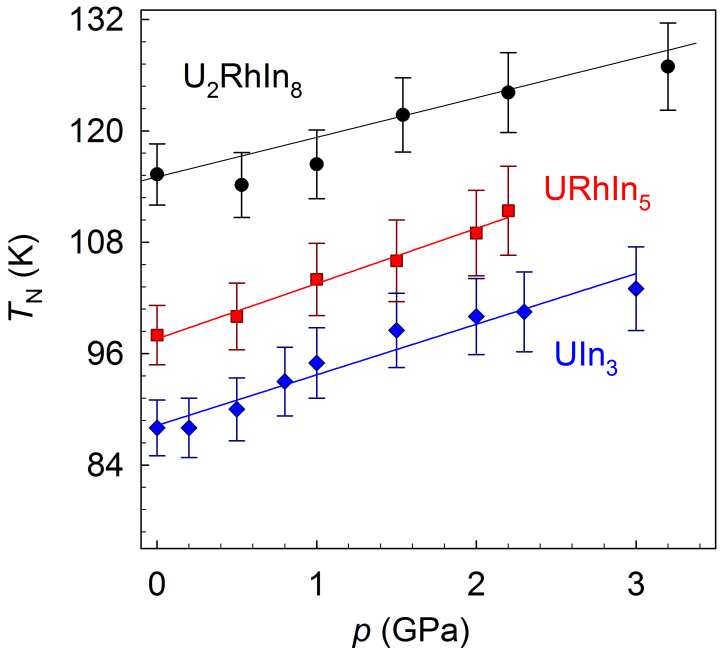

Figure 4.17: Temperature-pressure phase diagrams of UIn_3, $URhIn_5$ and U_2RhIn_8 compounds.

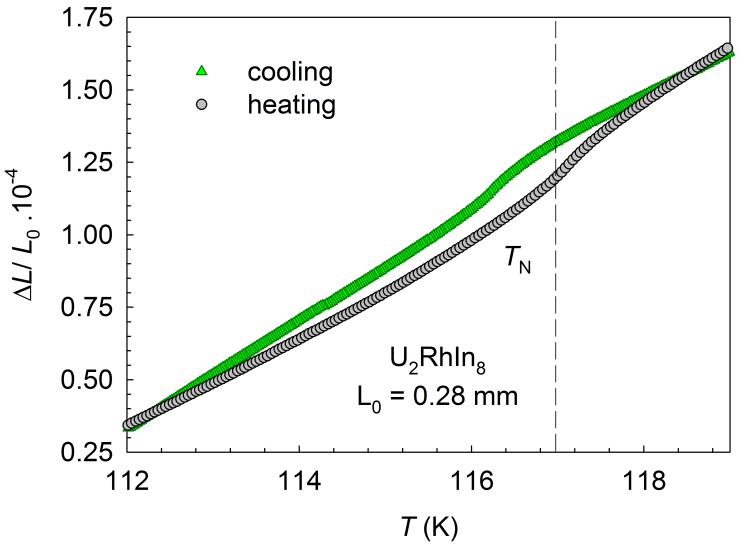

Figure 4.18: Relative length change of U_2RhIn_8 measured parallel to c-axis during heating/cooling. Vertical line shows the position of the Néel temperature obtained from heat capacity measurements.

show a hysteresis around the transition temperature $T_N = 117$ K obtained from the heat capacity measurement (see Figure 4.18). Contrary to the heat capacity measurements, where the character of the peak at T_N corresponds to a typical 2^{nd}-order phase transition, results from dilatometry point to a 1^{st}-order character of the phase transition. The coefficient of linear thermal expansion $\alpha(T) =$

$\frac{1}{l}\frac{\partial l}{\partial T}$ was calculated as a numerical derivative of relative length change with the temperature.

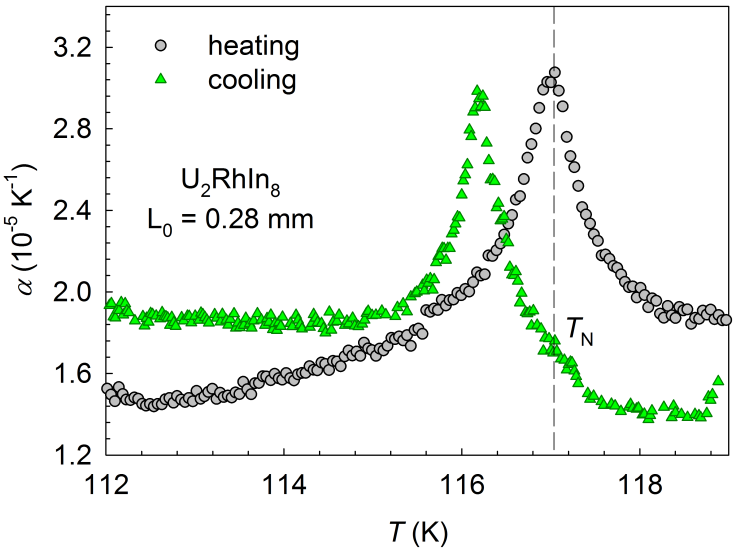

Figure 4.19: Temperature dependence of the coefficient of linear thermal expansion during heating/cooling of U_2RhIn_8 obtained as a numerical differentiation of relative length change with temperature. Vertical line shows the position of the Néel temperature obtained from the heat capacity measurements.

Since heat capacity measurements pointed to a 2nd-order phase transition in U_2RhIn_8, results from the thermal expansion measurements were analyzed with respect to the Ehrenfest relations for the 2nd-order phase transition [131]:

$$\frac{\partial T_N}{\partial p} = V_{mol} \cdot \frac{\Delta\alpha}{\Delta(C/T)} \tag{4.1}$$

where V_{mol} is the molar volume, $\Delta\alpha$ is the jump in the temperature dependence of the coefficient of linear thermal expansion and $\Delta(C/T)$ represents the jump in the heat capacity data (see Figure 4.20). The measurements of thermal expansion and heat capacity at ambient pressure allow a qualitative estimation of the slope of the change of T_N with applied hydrostatic pressure. Better agreement with experiment is obtained when assuming that the change in the coefficient of the linear thermal expansion is the same in all directions of the tetragonal lattice.

Results from thermal expansion measurements, on the other hand, indicated a 1st-order phase transition with a small hysteresis around $T_N = 117$ K (see Figure 4.18). Building on that premise we further analyzed the results with respect to Clausius-Clapeyron relation appropriate for a 1st-order phase transition:

$$\frac{\partial T_N}{\partial p} = \frac{\Delta V}{\Delta S}, \tag{4.2}$$

where ΔV is the volume change and ΔS is the jump in the magnetic entropy around the transition temperature (see Figure 4.21). Since measurements of thermal expansion could be performed only in the [001] direction, the volume change

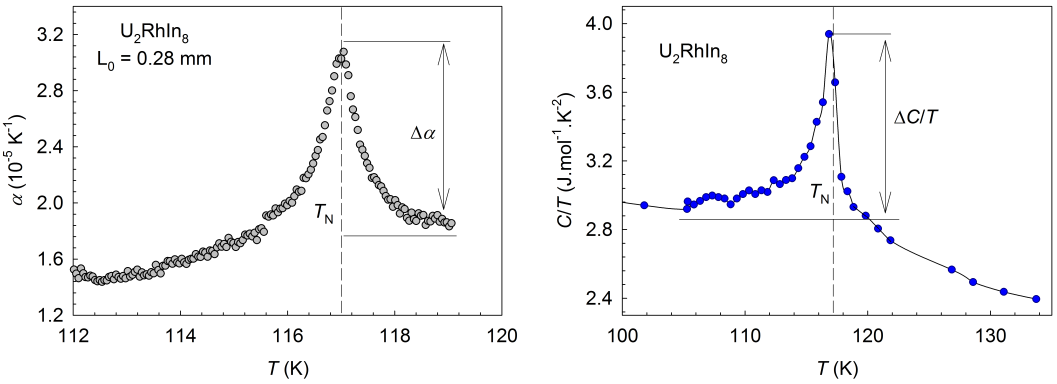

Figure 4.20: Estimation of the jump in the coefficient of linear thermal expansion (left figure) during heating and the jump estimated from heat capacity data for U_2RhIn_8 (right figure). Vertical line shows the position of the Néel temperature obtained from the heat capacity measurements.

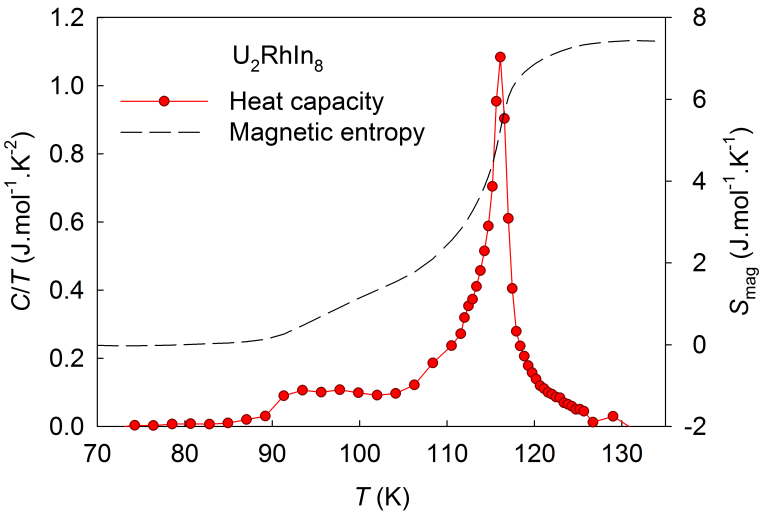

Figure 4.21: Temperature dependence of heat capacity around the transition temperature and jump in the magnetic entropy calculated as $\Delta S = \int \frac{C}{T} dT$.

was calculated assuming that the relative length change in the [100] direction is similar (isotropic volume change approximation).

The results from Ehrenfest and Clausius-Clapeyron relations are listed in Table 4.6 and compared to the result obtained from the direct measurement of temperature dependence of electrical resistivity under applied hydrostatic pressure. The direct comparison of the results points to a 1st-order phase transition in U_2RhIn_8 which is to be confirmed by heat pulse measurements using the PPMS apparatus.

	$\partial T_N/\partial p$ (K·GPa^{-1})
Ehrenfest	0.5
Isotropic Ehrenfest	1.5
Clausius-Clapeyron	3.3
Experiment	5.4

Table 4.6: The slope of the change of T_N with applied hydrostatic pressure from Ehrenfest relation, isotropic Ehrenfest relation, Clausius-Clapeyron relation and direct measurement.

4.3.4 Neutron diffraction

Single crystals of $URhIn_5$ were carefully selected for elastic neutron scattering measurement on the PANDA instrument. The selection procedure included the confirmation of desired composition and homogeneity by EDX analysis and orientation by Laue method. Crystals with the best quality were then glued with GE-varnish to thin aluminum plates (to minimize the background during neutron diffraction) (see Figure 4.22) with the crystals' c-axis perpendicular to the plate and with the a-axis parallel to the other crystals. The total mass of the single crystals was $8 \sim 10$ mg per each plate. Recent experiments of zero-field nuclear

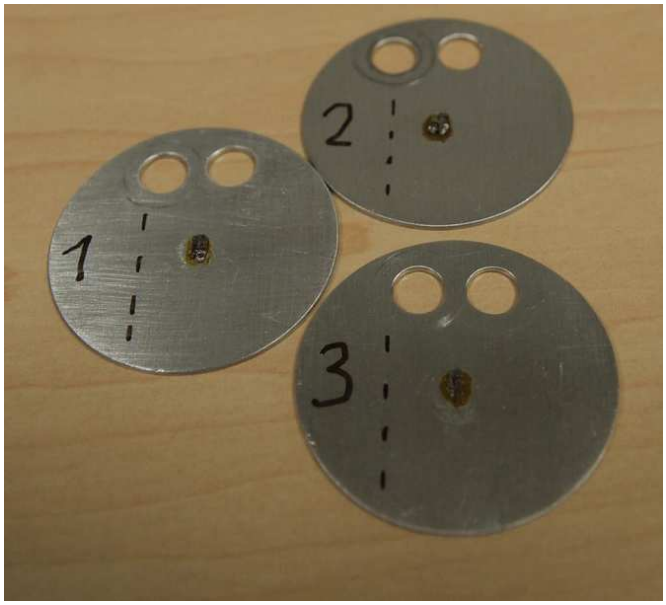

Figure 4.22: Aluminum plates with single crystals of $URhIn_5$ glued to its surface in [001] orientation.

magnetic resonance and nuclear quadrupole resonance on $URhIn_5$ [132] revealed all possible propagation vectors for this compound: $\boldsymbol{k} = (^1/_2, ^1/_2, 0)$, $\boldsymbol{k} = (^1/_2, ^1/_2, ^1/_2)$, $\boldsymbol{k} = (^1/_2, 0, ^1/_2)$ and $\boldsymbol{k} = (^1/_2, 0, 0)$.

By systematic searching around proposed positions in reciprocal space and mapping through the first Brillouin zone, we have found the magnetic Bragg satellites described by the propagation vector $\boldsymbol{k} = (^1/_2, ^1/_2, ^1/_2)$. Magnetic and nuclear reflections were collected in both the 'hot' and 'cold' region of PANDA with incident wave vectors $\boldsymbol{k}_i = 2.570$ Å^{-1} using pyrolytic graphite filter and $\boldsymbol{k}_i = 1.57$ Å^{-1} using beryllium filter, respectively. In total, 8 independent mag-

netic reflections have been measured, 5 of them had huge background and thus low quality. Figure 4.23 shows the comparison of intensities of measured and calculated reflections in FullProf software.

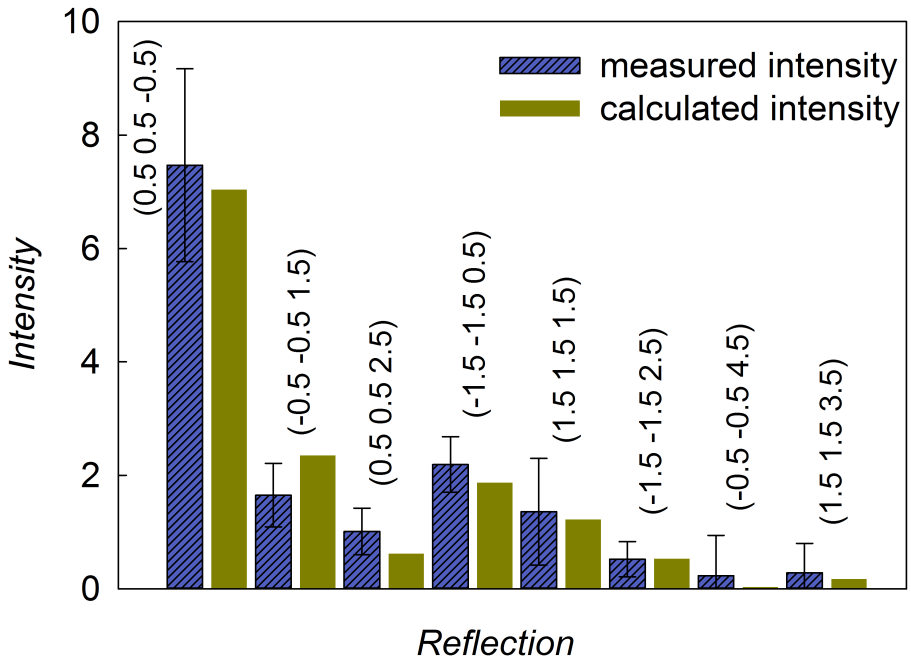

Figure 4.23: Comparison of intensities of measured and calculated reflections in FullProf software.

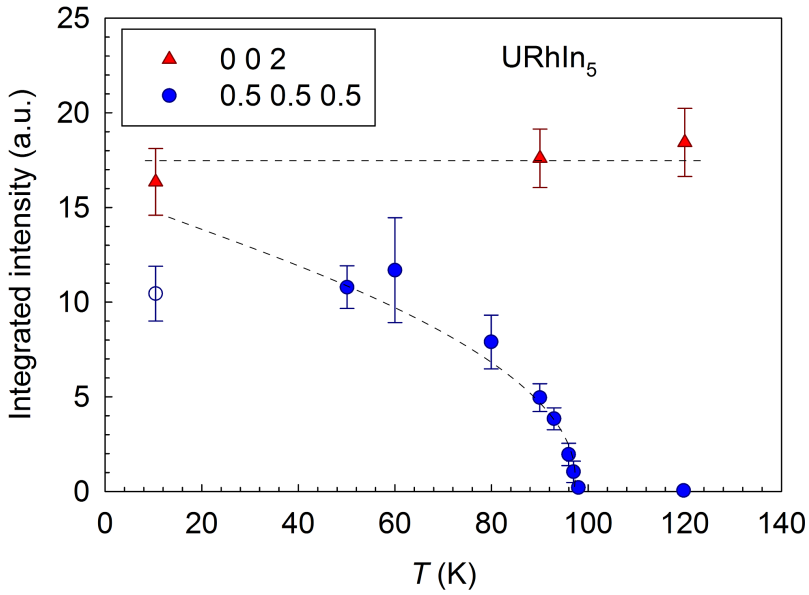

Figure 4.24: Temperature dependence of one nuclear and one magnetic reflection. The experimental point at the lowest measured temperature, in the case of the magnetic reflection, was not included in the fit.

Temperature dependence of the intensity of one nuclear (h k l) = (0 0 2) and one magnetic reflection (h k l) = (0.5 0.5 0.5) was measured (see Figure 4.24). The nuclear intensities do not change with temperature, confirming the absence of ferromagnetically coupled sublattices below T_{N}. For the magnetic reflection, the data were fitted to the power law $I \propto (T_N - T)^{2\beta}$ [133] resulting in $\beta = 0.23$ as an order parameter. This value suggests a 3D character of magnetic ordering.

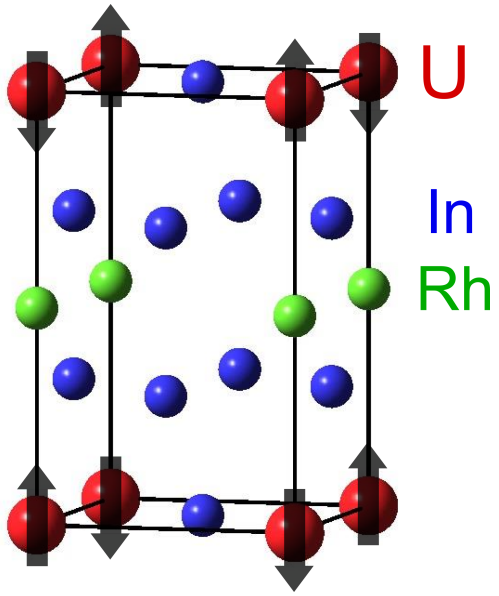

Figure 4.25: Magnetic structure of $URhIn_5$ obtained from the neutron diffraction measurement. Arrows depict the moments on uranium atoms.

Although the number of identified magnetic reflections was relatively small, it was enough for the magnetic structure determination (see Figure 4.25) and a rough estimation of magnetic moments. The magnetic moment per uranium site is $\mu = 1.65 \pm 0.11\ \mu_{\mathrm{B}}$.

4.3.5 Theoretical calculations

The spin-polarized LSDA calculation splits the spin-up and spin-down bands with spin magnetic moment at uranium site 2.17 μ_{B}. Since strong magnetocrystalline anisotropy is present, the spin-orbit coupling is also included into calculations. The calculated spin magnetic moment at uranium site decreases to $M_{\mathrm{S}} = 1.744\ \mu_{\mathrm{B}}$ and the orbital magnetic moment M_{L} = -2.418 μ_{B} is antiparallel. Magnetic moments located at rhodium and indium sites are both smaller than 0.1 μ_{B}. Total uranium magnetic moment is $|M_{\mathrm{T}}| = 0.674\ \mu_{\mathrm{B}}$. From comparison with $URhIn_5$ we expected larger total uranium moment about $|M_{\mathrm{T}}| = 1.6\ \mu_{\mathrm{B}}$. Thus, the correlation movement of $5f$ electrons is not negligible. Therefore we used LSDA+U method to describe correlated movement of $5f$ electrons. Tuning effective Hubbard U we have found spin magnetic moment $M_{\mathrm{S}} = 1.738\ \mu_{\mathrm{B}}$ and orbital magnetic moment M_{L} = -3.3 μ_{B} providing the total magnetic moment $|M_{\mathrm{T}}| = 1.592\ \mu_{\mathrm{B}}$ for medium effective $U = 1.3$ eV. In the case of $URhIn_5$ the total magnetic moment resulted in $|M_{\mathrm{T}}| = 1.618\ \mu_{\mathrm{B}}$ for the effective $U = 1.5$ eV. We are fully aware that such calculation loses its first-principle character on this level, but on the other hand, we show that these heuristically derived values of effective U allow us to obtain valuable results. The value of total magnetic moment on uranium site in $URhIn_5$ corresponds to the one obtained from neutron diffraction measurements $\mu = 1.65 \pm 0.11\ \mu_{\mathrm{B}}$/U.

Conclusions

In the presented work, we focused our attention on the $5f$ magnetism of new uranium compounds which have a crystal structure identical to the well known cerium-based superconductors such as $CeCoIn_5$ [5] and Ce_2CoIn_8 [8]. Single crystals of UIn_3, $URhIn_5$ and the novel U_2RhIn_8 phase were synthesized using the In self-flux method and characterized by the microprobe analysis and various X-ray diffraction methods (single crystal, powder and Laue diffraction) and their properties were studied by both macroscopic (magnetization, heat capacity, electrical resistivity and thermal expansion subjected to high magnetic fields up to 9 T and hydrostatic pressures up to 3.2 GPa) and microscopic (neutron diffraction) measurements. The U_nRhIn_{3n+2} compounds adopt the layered tetragonal Ho_2CoGa_{3n+2} ($n = 1, 2$) structure type with a space group P4/mmm; UIn_3 crystallizes in the cubic $AuCu_3$-type structure with a $Pm\bar{3}m$ space group. The structure consists of UIn_3 'blocks' and TIn_2 stacked sequentially along the tetragonal c-axis.

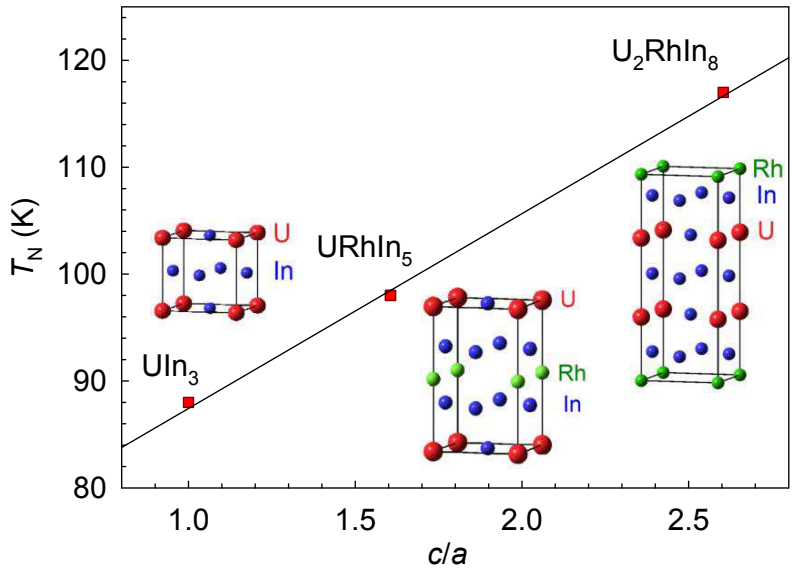

Figure 4.26: T_N vs. c/a diagram depicting the evolution of transition temperature with respect to increasing c/a ratio. The points are accompanied by the structures UIn_3 (cubic), $URhIn_5$ (tetragonal) and U_2RhIn_8 (tetragonal) compounds. Solid black line is a guide to the eye.

All three uranium compounds undergo a transition into the antiferromagnetic state at $T_N = 88$ K for UIn_3, $T_N = 98$ K for $URhIn_5$ and $T_N = 117$ K for U_2RhIn_8. The Néel temperature increases with increasing c/a ratio (see Figure 4.26). Electrical resistivity measurement revealed the very high quality of the studied ternary compounds with RRR exceeding 200 and 500, respectively. Near the transition temperature a tiny kink is observed, accompanied by a 2^{nd}-order-like phase transition and a formation of a gap at the Fermi surface. The temperature dependence of magnetic susceptibility for $URhIn_5$ and U_2RhIn_8 reveals a strong magnetic anisotropy and suggests that both systems undergo

an itinerant-localized crossover at high temperatures above 300 K, similar to other uranium-based compounds (UPd_2Al_3, URu_2Si_2 [125]), including $UPtGa_5$ [125] from the same group of compounds. According to the heat capacity measurements, the antiferromagnetic order is very resistant against the application of external magnetic field up to 9 T. The application of the hydrostatic pressure supports the robustness of the antiferromagnetic phase in both ternary compounds with similar pressure coefficients [1]. The gradual increase of T_N in these compounds can be explained using spin-fluctuation theory of an itinerant $5f$ electron system alongside with the Hubbard model [129, 130]. According to this scenario, hydrostatic pressure induces an increase in the hybridization between $5f$ and conduction electrons, which strengthens the exchange coupling J between U ions.

Thermal expansion measurement revealed a hysteresis around the Néel temperature which suggests a 1st-order phase transition in U_2RhIn_8. This is an unexpected result, as the heat capacity measurements point to a 2nd-order phase transition similar to $URhIn_5$ and UIn_3. This contradiction could be explained if we consider the difficulty of measuring the extremely narrow peak of the 1st-order transitions in the specific heat. The transition could be then missed even when performing several attempts. The order of transition was further analyzed with respect to the Ehrenfest and Clausius-Clapeyron relations. The experimental results from electrical resistivity under applied hydrostatic pressure show better correspondence with the theoretical prediction for the 1st-order phase transition (see Table 4.6) supporting our speculations.

Neutron diffraction measurement of $URhIn_5$ revealed the arrangement of magnetic moments with a propagation vector $\boldsymbol{k} = (1/2, 1/2, 1/2)$ and the determined magnetic moment per uranium ion is $\mu = 1.65 \pm 0.11\ \mu_B$. This commensurate structure differs from the incommensurate magnetic structure in the related $CeRhIn_5$ which is characterized by a propagation vector $\boldsymbol{k} = (1/2, 1/2, 0.297)$ in the ground state [7]. Microscopic measurements are needed to reveal the details of magnetic moment arrangements in U_2RhIn_8. A proposal has been successfully accepted for the magnetic structure determination of the U_2RhIn_8 compound on the D10 instrument at ILL, Grenoble.

The character of the structural dimensionality develops from 3D towards 2D when spanning the series: UIn_3 (1-0-3) $\rightarrow$ U_2RhIn_8 (2-1-8) $\rightarrow$ $URhIn_5$ (1-1-5) which makes it unique among related tetragonal $5f$ systems. In the other cases, either only the cubic compound (USn_3, UPb_3 [17]) or the cubic compound (UGa_3 [16]) together with its 1-1-5 (or 2-1-8) parent system (T = Fe, Co, Ni, Pd, Ir, Pt) are known [1, 19, 20, 22]. The Ga-based compounds with T = Fe, Rh, which form both 1-1-5 and 2-1-8, are paramagnetic. T_N vs. m/n diagram can be constructed, where m and n represent the number of $RhIn_2$ and (U,Ce)In_3 layers, respectively, for the investigated ternary compounds (see Fig. 4.27) in order to study the effect of stacking composition on the magnetic ordering. In contrast to the cerium compounds [134], the Néel temperatures of U_nRhIn_{3n+2} decrease with respect to the increasing m/n ratio. A possible explanation of the opposite behavior in both series is given by the different driving microscopic mechanisms in the compounds. These mechanisms in Ce-based compounds are mostly RKKY-type while in the uranium compounds the $5f$-ligand hybridization plays a substantial role. Moreover, the energy scales in both systems differ by

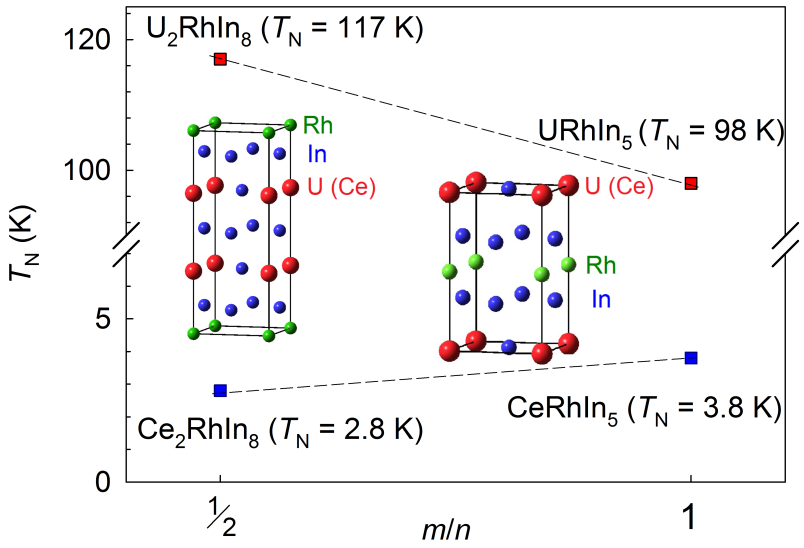

Figure 4.27: T_N vs. m/n diagram depicting the relationship of the stacking composition and magnetism of uranium layered structures in contrast to their cerium analogs. The points are accompanied by the tetragonal structures and transition temperatures of (U,Ce)$RhIn_5$ and (U,Ce)$_2RhIn_8$ compounds. Dashed black line is a guide to the eye.

two orders of magnitude, as the cerium-based compounds order magnetically well below 10 K while the ordering temperature in the case of U-based compounds exceeds 100 K. This behavior will be a subject of further investigation.

Bibliography

[1] Y. Matsumoto, Y. Haga, N. Tateiwa, H. Sakai, T. D. Matsuda, E. Yamamoto, Z. Fisk, *Phys. Rev. B* 88 (2013) 045120

[2] A. Bartha, M. Kratochvílová, M. Dušek, V. Sechovský, J. Custers, `http://arxiv.org/abs/1501.02150`

[3] A. Benoit, J. Boucherle, P. Convert, J. Flouquet, J. Palleau, J. Schweizer, *Solid State Commun.* 34 (1980) 293

[4] N. D. Mathur, F. M. Grosche, S. R. Julian, I. R. Walker, D. M. Freye, R. K. W. Haselwimmer, G. G. Lonzarich, *Nature* 394 (1998) 39

[5] R. Movshovich, M. Jaime, J. D. Thompson, C. Petrovic, Z. Fisk, P. G. Pagliuso, J. L. Sarrao, *Phys. Rev. Lett.* 86 (2001) 5152

[6] H. Hegger, C. Petrovic, E. G. Moshopoulou, M. F. Hundley, J. L. Sarrao, Z. Fisk, J. D. Thompson, *Phys. Rev. Lett.* 84 (2000) 4986

[7] W. Bao, P. G. Pagliuso, J. L. Sarrao, J. D. Thompson, Z. Fisk, J. W. Lynn and R. W. Erwin, *Phys. Rev. B* 62 (2001) 219901

[8] G. Chen, S. Ohara, M. Hedo, Y. Uwatoko, K. Saito, M. Sorai, I. Sakamoto, *J. Phys. Soc. Jpn.* 71 (2002) 2836

[9] J. D. Thompson, R. Movshovich, Z. Fisk, F. Bouquet, N. J. Curro, R. A. Fisher, P. C. Hammel, H. Hegger, M. F. Hundley, M. Jaime, P. G. Pagliuso, C. Petrovic, N. E. Phillips, J.L. Sarrao, *Journal of Magnetism and Magnetic Materials* 226 (2001) 5

[10] M. Nicklas, V. A. Sidorov, H. A. Borges, P. G. Pagliuso, C. Petrovic, Z. Fisk, J. L. Sarrao, J. D. Thompson, *Phys. Rev. B* 67 (2003) 020506(R)

[11] A. Schenck, F. N. Gygax, T. Ueda, Y. Ōnuki, *Phys. Rev. B.* 70 (2004) 054415

[12] Y. Tokiwa, H. Harima, D. Aoki, S. Nojiri, M. Murakawa, K. Miyake, N. Watanabe, R. Settai, Y. Inada, H. Sugawara, H. Sato, Y. Haga, E. Yamamoto and Y. Ōnuki, *J. Phys. Soc. Jpn.* 69 (2000) 1105

[13] G. W. Grabtree, B. D. Dunlap and D. D. Koelling, *Physica B* 135 (1985) 38

[14] Y. Tokiwa, D. Aoki, Y. Haga, E. Yamamoto, S. Ikeda, R. Settai, A. Nakamura and Y. Ōnuki, *J. Phys. Soc. Jpn.* 70 (2001) 3326

[15] A. Murasik, P. Fischer and Z. Zolnierek, *Physica B* 102 (1980) 188

[16] D. Kaczorowski, R. Hauser and A. Czopnik, *Physica B* 230-232 (1997) 35

[17] P. Boulet, H. Noël, *Solid State. Commun.* 107 (1998) 135

[18] Y. Haga, F. Honda, T. Eto, G. Oomi, T. Kagayama, N. Takeshita, N. Mori, T. Nakanishi, Y. Tokiwa, D. Aoki, Y. Ōnuki, *J. Phys. Soc. Jpn.* 71 (2002) 2019

[19] Y. N. Grin, P. Rogl, K. Hiebl, *J. Less-Common Met.* 121 (1986) 497

[20] S. Ikeda, Y. Tokiwa, T. D. Matsuda, A. Galatanu, E. Yamamoto, A. Nakamura, Y. Haga, Y. Ōnuki, *Physica B* 359 (2005) 1039

[21] K. Kaneko, N. Metoki, N. Bernhoeft, G. H. Lander, Y. Ishii, S. Ikeda, Y. Tokiwa, Y. Haga, Y. Ōnuki, *Phys. Rev. B* 68 (2003) 214419

[22] S. Ikeda, T. Ōkubo, Y. Inada, Y. Tokiwa, K. Kaneko, T. D. Matsuda, E. Yamamoto, Y. Haga, Y.Ōnuki, *J. Phys.: Condens. Matter* 15 (2003) 2015

[23] Stephen Blundell, Magnetism in Condensed Matter, Oxford University Press Inc., New York 2001, ISBN: 0-19-850592-2.

[24] W. N. Cottingham, D. A. Greenwood, Electricity and Magnetism, Cambridge University Press 1991, ISBN: 0521368030

[25] C. P. Poole, H. A. Farach, R. J. Creswick, R. Prozorov, Superconductivity, Elsevier Academic Press 2007, ISBN: 978-0-12-088761-3

[26] W. Meissner, R. Ochsenfeld, *Naturwissenschanften* 21 (1933) 787-788

[27] V. Nekvasil, M. Diviš, Localized $4f$ and $5f$ Moments: Magnetism in Encyclopedia of Materials: Science and Technology edited by K. H. J. Buschow *et al.* (2001) 4613

[28] L. Havela, $5f$ Electron Systems: Magnetic Properties in Encyclopedia of Materials: Science and Technology edited by K. H. J. Buschow *et al.* (2001) 2584

[29] Radial wave functions from http://ej.iop.org/images

[30] K. W. H. Stevens, *Proc. Phys. Soc. A* 65 (1952) 209

[31] D. I. Khomskii, Transition Metal Compounds, Cambridge University Press 2014, ISBN: 9781107020177

[32] W. Pauli, *Z. Phys.* 41 (1927) 81

[33] F. Bloch, *Z. Phys.* 57 (1929) 545

[34] E. C. Stoner, *Proc. Roy. Soc. A* 154 (1936) 656

[35] E. P. Wolfrath, *Iron, Cobalt and Nickel*, In *Ferromagnetic Materials*, Vol. 1, North-Holland, Amsterdam 1980

[36] J. Kübler, Itinerant electron magnetism, Oxford University Press Inc., New York 2000, ISBN: 0-19-850028-9

[37] R. G. Parr and W. Yang, Density Functional Theory of Atoms and Molecules, Oxford University Press Inc., New York 1989, ISBN: 0-19-504279-4

[38] M. A. Ruderman, C. Kittel, *Phys. Rev.* 96 (1954) 99

[39] T. Kasuya, *Prog. Theor. Phys.* 16 (1956) 45

[40] K. Yoshida, *Phys. Rev.* 106 (1957) 893

[41] P. Čermák, P. Javorský, M. Kratochvílová, K. Pajskr, M. Klicpera, B. Ouladdiaf, M.-H. L.-Cailleau, J. Rodriguez-Carvajal and Martin Boehm, *Phys. Rev. B* 89 (2014) 184409

[42] G. Busch and O. Vogt, *Journal of the Less-Common Metals* 62 (1978) 335

[43] L. Lundgren, P. Svedlindh, P. Nordblad and O. Beckman, *Phys. Rev. Lett.* 51 (1983) 911

[44] B. Coqblin: Electron Systems: Strong Correlations in Encyclopedia of Materials: Science and Technology, edited by K. H. J. Buschow et al., (2001) p.2591-2603, Elsevier, Oxford

[45] J. Kondo, *Prog. Theor. Phys.* 32 (1964) 37

[46] V. Sechovský: General Introduction: in Encyclopedia of Materials: Science and Technology, edited by K.H.J Buschow et al., p.5018, (2001) Elsevier, Oxford

[47] K. Andres, J. E. Graebner, H. R. Ott, *Phys. Rev. Lett.* 35 (1975) 1779

[48] P. Coleman, A. J. Schofield, *Nature*, 433 (2005) 226

[49] W. Heisenberg, *Z. Phys.* 43 (1927) 172

[50] F. Steglich, J. Aarts, C. D. Bredl, W. Lieke, D. Meschede, W. Franz, H. Schäfer, *Phys. Rev. Lett.* 43 (1979) 1892

[51] J. Bardeen, L. N. Cooper, J. R. Schrieffer, *Phys. Rev.* 108 (1957) 1175

[52] P. Monthoux, D. Pines, G. G. Lonzarich, *Nature* 450 (2007) 1177

[53] T. Park, V. A. Sidorov, F. Ronning, J.-X. Zhu, Y. Tokiwa, H. Lee, E. D. Bauer, R. Movshovich, J. L. Sarrao, J. D. Thompson, *Nature* 456 (2008) 366

[54] T. Park, F. Ronning, H. Q. Yuan, M. B. Salomon, R. Movshovich, J. L. Sarrao, J. D. Thompson, *Nature* 440 (2006) 65

[55] H. v. Löhneysen: Non-Fermi Liquid Behaviour: Quantum Phase Transition In Encyclopedia of Materials: Science and Technology, edited by K.H.J. Buschow et al., (2001) p.6185-6191, Elsevier, Oxford

[56] G. R. Stewart, *Review of Modern Physics* 73 (2001) 797

[57] G. Knebel, D. Aoki, D. Braithwaite, B. Salce, J. Flouquet, *Phys. Rev. B* 74 (2006) 020501(R)

[58] J. A. Hertz, *Physical Review B*, 14 (1976) 1165

[59] A. J. Millis, *Physical Review B* 48 (1993) 7183

[60] T. Moriya, T. Takimoto, *Journal of the Physical Society of Japan* 64 (1995) 960

[61] G. G. Lonzarich, *Electron*, Cambridge University Press, 1997

[62] P. W. Anderson, *Phys. Rev.* 124 (1961) 41

[63] S. Doniach, *Physica B* 91 (1977) 231

[64] J. R. Iglesias, C.Lacroix, B. Coqblin, *Phys. Rev. B* 56 (1997) 11820

[65] J. Custers, Quantum-Critical Behavior in the Heavy-Fermion Compounds $YbRh_2Si_2$ and $CeIn_{3-x}Sn_x$, dissertation, 2004

[66] V. Sechovský, L. Havela, Magnetism of ternary intermetallic compounds of uranium in Encyclopedia of Materials: Science and Technology edited by K. H. Buschow *et al.* (2001)

[67] H. H. Hill, Plutonium 1970 and other actinides, AIME, New York (1970), p. 2

[68] V. Sechovský, Z. Smetana, G. Hilscher, E. Gratz, H. Sassik, *Physica B* 102 (1980) 277

[69] D. D. Koelling, B. D. Dunlap, G. W. Grabtree, *Phys. Rev. B* 31 (1985) 4966

[70] M. S. S. Brooks, P. J. Kelly, *Phys. Rev. Lett.* 51 (1983) 1709

[71] H. B. Callen, Thermodynamics and an Introduction to Thermostatistics, 2^{nd} ed. (1985) John Wiley & Sons Inc.

[72] SSE II (Solid State Electrontransport): Užívatelský manuál řídícího systému, MFF UK Praha 2001

[73] W. Bardsley *et al.*, Crystal Growth: a Tutorial approach 2, North-Holland, New-York (1970) ISBN: 0444853715

[74] R. Abbaschian: Crystal growth in Encyclopedia of Materials: Science and Technology, edited by k. H. J. Buschow *et al.*, Elsevier, Oxford (2001) p.1860

[75] `http://www.esrf.eu/`

[76] V. Valvoda, M. Polcarová, P. Lukáč: Základy strukturní analýzy, Karolinum (1992) Praha, ISBN:80-200-0280-4

[77] N. W. Ashcroft, N. D. Mermin: Solid State Physics, Thomson Learning (1976) ISBN: 0-03-083993-9

[78] http://www.photonic-science.com/

[79] http://www.bruker.com/

[80] J. Rodriguez-Carvajal, *Physica B: Condensed Matter*, 192(1-2):55-69, 1993

[81] T. Roisnel and J. Rodriguez-Carvajal, Winplotr: a windows tool for powder diffraction patterns analysis. In R. Delhez and E.J. Mittemeijer, editors, *EPDIC 7 - Seventh European Powder Diffraction Conference*, Trans Tech Publications.

[82] H. Rietveld, *Journal of Applied Crystallography* 2(2):65-71, 1969.

[83] http://kfkl.cz/

[84] http://www.cas.cz/

[85] http://www.rigaku.com/smc/spider.html

[86] http://www.crystalclearsoftware.com/

[87] L. Palatinus, G. Chapuis, *J. Appl. Cryst.* 40 (2007) 786

[88] V. Petricek, M. Dusek and L. Palatinus, *Z. Kristallogr.* 229(5) (2014) 345

[89] http://www.tescan.com

[90] http://www.bruker.com

[91] http://www.pharmacopeia.cn/v29240/images/v29240/g-1092.gif

[92] http://www.qdusa.com/

[93] J. Sh. Hwang, K. J. Lin and Ch. Tien, *Rev. Sci. Instrum.* 68 (1), (1997) 94

[94] http://en.wikipedia.org/wiki/Phonon

[95] P. Svoboda, private communications

[96] C. A. Martin, *Journal of Phys.: Condens. Matter* 3 (1991) 5967

[97] N. H. Andersen, *Phys. Rev. B* 19 (1979) 384

[98] M. B. Fontes, J. C. Trochez, B. Giordanengo, S. L. Buďko, D. R. Sanchez, E. M. Baggio-Saitovitch and M. A. Continentino, *Phys. Rev. B* 60 (1999) 6781

[99] N. Fujiwara, T. Matsumoto, K. Koyama-Nakazawa, A. Hisada, Y. Uwatoko, *Rev. Sci. Instrum.* 78 (2007) 073905

[100] K. Murata, H. Yoshino, H. O. Yudav, Y. Honda and N. Shirakawa, *Rev. Sci. Instrum.* 68 (1997) 2490

[101] Y. Uwatoko, M. Hedo, N. Kurita, M. Koeda, M. Abliz, T. Matsumoto, *Physica B* 329-333 (2003) 1658

[102] B. D. Josephson, *Physics Letters* 1 (1962) 251

[103] Y. S. Touloukian, Thermophysical Properties of Matter: Thermal expansion: metallic elements and alloys, by Y. S. Touloukian and others (1970) IFI/Plenum

[104] C. Y. Ho, R.E. Taylor, Thermal Expansion of Solids (1988) Asm International

[105] Ch Bittorf, S. Matthies, H. G. Priesmeyer, R. Wagner, *Intermetallics* 7 (1999) 251

[106] J. N. Fox, *American Journal of Physics* 58 (1990) 875

[107] J. Valentich, *Journal of Materials Science* 14 (1979) 371

[108] J. D. James, J. A. Spittle, S. G. R. Brown, R. W. Evans, *Measurement Science and Technology* 12 (2001) R1

[109] H. Müller, M. Rotter, Capacitance Dilatometer DIL20-11 - Users Manual (2012)

[110] R. Pott, R. Schefzyk, *Journal of Physics E: Scientific Instruments* 16 (1983) 444

[111] C. R. Tilford, C. A. Swenson, *Physical Review B* 5 (1972) 719

[112] V. F. Sears, Neutron News 3 (1992) 26

[113] P. Čermák, Magnetic properties of R_2TIn_8 and related tetragonal compounds, 2014. Phd thesis, Charles University

[114] `http://www.frm2.tum.de/`

[115] `http://nmi3.eu/neutron-research/techniques-for-/dynamics`

[116] M. Diviš, lecture notes

[117] W. Zu, R. E. Cohen, *Phys. Rev. B* 73 (2006) 235116

[118] J. P. Perdew, K. Burke, M. Ernzerhof, *Phys. Rev. Lett.* 77 (1996) 3865

[119] M. Diviš, *Physica B* 407 (2012) 2524

[120] X. R. Huang, *J. Appl. Cryst.* 43 (2010) 926

[121] M. E. Fisher, *Philosophical Magazine* 82 (1962) 1731

[122] H. Sakai, S. Kambe, Y. Tokunaga, Y. Matsumoto, N. Tateiwa, Y. Haga, Z. Fisk, *Phys. Rev. B* 88 (2013) 045123

[123] J. R. Thompson, S. T. Sekula, C. - K. Loong, C. Stassis, *J. Appl. Phys. 53* (1982) 7893

[124] R. M. Galera, A. P. Murani, J. Pierre, K. R. A. Ziebeck, *J. Magn. Magn. Mater. 63 & 64* (1987) 594

[125] A. Galatanu , Y. Haga, T. D. Matsuda, S. Ikeda, E. Yamamoto, D. Aoki, T. Takeuchi and Y. Ōnuki, *J. Phys. Soc. Jpn.* 74 (2005) 1582

[126] A. C. Hewson, *The Kondo Problem to Heavy Fermions*, ISBN: 0-521-36382-9, Cambridge University Press 1993

[127] N. Tateiwa, S. Ikeda, Y. Haga, T. D. Matsuda, E. Yamamoto, K. Sugiyama, M. Hagiwara, K. Kindo and Y. Ōnuki, *J. Phys. Soc. Jpn.* 80 (2011) 014706 and references therein

[128] K. Kadowaki, S. B. Woods, *Solid State Commun.* 58 (1986) 507

[129] B. R. Cooper, Q. G. Sheng, U. Benedict, P. Link, *J. Alloys Compd.* 213-214 (1994) 120

[130] Q. G. Sheng, B. R. Cooper, *J. Magn. Magn. Mater.* 164 (1996) 335

[131] J. Rohrkamp, O. Heyer, T. Fickenscher, R. Pöttgen, S. Jodlauk, H. Hartmann, T. Lorenz, J. A. Mydosh, *Journal of Phys.: Condens. Matter* 19 (2007) 48

[132] H. Sakai, S. Kambe, Y. Tokunaga, Y. Matsumoto, N. Tateiwa, Y. Haga, Z. Fisk, *Phys. Rev. B* 88 (2013) 045123

[133] G. S. Brush, *Rev. Mod. Phys.* 39 (1967) 883

[134] A. L. Cornelius, P.G. Pagliuso, M. F. Hundley and J. L. Sarrao, *Phys. Rev. B* 64 (2001) 144411

List of Tables

List of Figures